

Experimental and Theoretical Study of the Carbon-13 and Deuterium Kinetic Isotope Effects in the Cl and OH Reactions of CH₃F

Marina Marinkovic,[†] Margret Gruber-Stadler,^{†,‡} J. Michael Nicovich,[§] Raenell Soller,^{||} Max Mühlhäuser,[‡] Paul H. Wine,^{§,||} Lihn Bache-Andreassen,[†] and Claus J. Nielsen^{*,†}

Centre for Theoretical and Computational Chemistry, Department of Chemistry, University of Oslo, P.O. Box. 1033, Blindern 0315 Oslo, Norway, Studiengang Umwelt-, Verfahrens- & Biotechnik, MCI—Management Center Innsbruck Internationale Fachhochschulgesellschaft mbH, Egger-Lienz-Strasse 120, A-6020 Innsbruck, Austria, and School of Chemistry and Biochemistry and School of Earth and Atmospheric Sciences, Georgia Institute of Technology, Atlanta, Georgia 30332

Received: August 26, 2008; Revised Manuscript Received: September 20, 2008

A laser flash photolysis–resonance fluorescence technique has been employed to determine absolute rate coefficients for the CH₃F + Cl reaction in N₂ bath gas in the temperature range of 200–700 K and pressure range of 33–133 hPa. The data were fitted to a modified Arrhenius expression $k(T) = 1.14 \times 10^{-12} \times (T/298)^{2.26} \exp\{-313/T\}$. The OH and Cl reaction rates of ¹³CH₃F and CD₃F have been measured by long-path FTIR spectroscopy relative to CH₃F at 298 ± 2 K and 1013 ± 10 hPa in purified air. The FTIR spectra were fitted using a nonlinear least-squares spectral fitting method including line data from the HITRAN database and measured infrared spectra as references. The relative reaction rates defined by $\alpha = k_{\text{light}}/k_{\text{heavy}}$ were determined to be $k_{\text{OH}+\text{CH}_3\text{F}}/k_{\text{OH}+\text{CD}_3\text{F}} = 4.067 \pm 0.018$, $k_{\text{OH}+\text{CH}_3\text{F}}/k_{\text{OH}+^{13}\text{CH}_3\text{F}} = 1.067 \pm 0.006$, $k_{\text{Cl}+\text{CH}_3\text{F}}/k_{\text{Cl}+\text{CD}_3\text{F}} = 5.11 \pm 0.07$, and $k_{\text{Cl}+\text{CH}_3\text{F}}/k_{\text{Cl}+^{13}\text{CH}_3\text{F}} = 1.016 \pm 0.006$. The carbon-13 and deuterium kinetic isotope effects in the OH and Cl reactions of CH₃F have been further investigated by quantum chemistry methods and variational transition state theory.

1. Introduction

Isotopes are frequently employed in studies of chemical reactions to distinguish between alternative mechanisms. In chemical kinetic studies, the isotope effects (KIEs) give additional information about the potential energy surface of the reaction and serve as benchmarks in quantum chemistry descriptions. Experimental KIEs are available for the radical reactions of the key atmospheric compounds CH₄,^{1–3} HCHO,^{4,5} and CO^{6,7} (and references therein). Data are also available for a few halogenated C₁-compounds such as CH₃Cl,^{8,9} CHCl₃,¹⁰ CH₃I,¹¹ and CH₃OH.¹²

Fluoromethane (CH₃F, Freon 41, HFC 41, F 41, R 41) is presently not of environmental concern, but, being the simplest HFC, it has served as both a standard and a mimic of larger HFCs and has been the subject of several studies reporting kinetic results from the reaction with OH radicals^{13–19} and Cl atoms.^{20–24} The data have been critically reviewed and the current JPL recommendations²⁵ are $k(T)_{\text{OH}+\text{CH}_3\text{F}} = 2.5 \times 10^{-12} \times e^{-1430/T}$ and $k(T)_{\text{Cl}+\text{CH}_3\text{F}} = 1.96 \times 10^{-11} \times e^{-1200/T}$. The current IUPAC recommendations²⁶ are $k(T)_{\text{Cl}+\text{CH}_3\text{F}} = 4.0 \times 10^{-12} \times e^{-730/T}$ in the temperature range of 240–370 K and $k(T)_{\text{OH}+\text{CH}_3\text{F}} = 1.9 \times 10^{-12} \times e^{-1350/T}$ in the temperature range of 240–300 K or a three-parameter fit $k(T)_{\text{OH}+\text{CH}_3\text{F}} = 3.66 \times 10^{-18} \times T^2 \times e^{-818/T}$ in the temperature range of 243–393 K. Likewise, several quantum chemical modeling studies have been

published for the fluoromethane reactions with Cl atoms^{27–29} and OH radicals.^{30–35}

2. Experimental and Computational Methods

2.1. Reference Spectra and Relative Rate Experiments.

The experiments were carried out in a 250 L electropolished stainless steel smog chamber equipped with a White type multiple reflection mirror system with a 120 m optical path length for rovibrationally resolved infrared spectroscopy. The infrared spectra were recorded with a Bruker IFS 66v FTIR instrument employing an InSb detector. The reaction chamber is equipped with UV photolysis lamps mounted in a quartz tube inside the chamber, and all experiments were carried out in synthetic air (AGA 99.99%; CH₄, CO, and NO_x < 100 ppbv) at 298 ± 2 K and 1013 ± 10 hPa. Each of the Cl and OH experiments was carried out several times for different mixtures of CH₃F + CD₃F and CH₃F + ¹³CH₃F. Initial partial pressures of the fluoromethane isotopologues were in the range of 0.1–1.5 Pa and the cell was filled to 1013 hPa with synthetic air (99.99%, AGA). As a standard, 128 scans were coadded at a nominal resolution of 0.125 cm⁻¹ and Fourier transformed using boxcar apodization. The kinetic experiments were programmed with periods of data collection (ca. 4 min) alternated with UV photolysis and a waiting period of 2 min.

CH₃F (99%, Fluorochem), CD₃F (>99.9 atom% D, CDN Isotopes), and ¹³CH₃F (99% and 90%, ICON) were used as received without further purification. Hydroxyl radicals were generated by photolysis of O₃ in the presence of H₂ (99%, AGA). Ozone was produced from oxygen (99.995%, AGA) using a MK II ozone generator from BOC, which has a conversion efficiency of approximately 5%, and was collected in a trap filled with silica beads at 195 K. Typical partial pressures of ozone and hydrogen were 50 and 200 Pa,

* Corresponding author. Tel: +47 2285 5680. Fax: +47 2285 5441. E-mail: claus.nielsen@kjemi.uio.no.

[†] University of Oslo.

[‡] MCI—Management Center Innsbruck Internationale Fachhochschulgesellschaft mbH.

[§] School of Chemistry and Biochemistry, Georgia Institute of Technology.

^{||} School of Earth and Atmospheric Sciences, Georgia Institute of Technology.

respectively. Photolysis of ozone was carried out at intervals of 10–15 min using a Philips TUV 30W lamp ($\lambda_{\text{max}} \sim 254$ nm). This OH production method produces not only OH radicals in the ground-state but also in excited vibrational states.^{36–38} The collision quenching rate coefficients of OH by N₂ and O₂ is on the order of 10^{-15} and 10^{-13} cm³ molecule⁻¹ s⁻¹, respectively.³⁹ As the mixing ratios of O₂ and N₂ are 4 orders of magnitude larger than those of the fluoromethane isotopologues, one may safely assume that these react exclusively with OH in the vibrational ground state.

Chlorine atoms were generated by photolysis of molecular chlorine (2–3 Pa; 99.8%, AGA) at intervals of 1–10 min by employing a Philips TUV 30 W lamp ($\lambda_{\text{max}} \sim 254$ nm). The use of this lamp was preferred, as it will also photolyze HC(O)F and CH₂FOOH produced in the degradation of CH₃F; see later discussion. At these short wavelengths, Cl atoms can be formed in the excited spin-orbit state ²P_{1/2}, which is 882 cm⁻¹ above the ground state ²P_{3/2}. The quenching rate coefficients of Cl(²P_{1/2}) by O₂ and N₂ are on the order of 10^{-13} and 10^{-15} cm³ molecule⁻¹ s⁻¹.⁴⁰ The mixing ratios of O₂ and N₂ are 4 orders of magnitude larger than that of CH₃F, and we assume that only Cl(²P_{3/2}) will react with CH₃F, which is supported by a recent study of the reactivity of thermalized Cl atoms toward CH₃F and other organic compounds.²¹

The kinetic study was carried out by the relative rate method in a static gas mixture, in which the removals of the reacting species are measured simultaneously as a function of reaction time. Assuming that the reactants react solely with the same radical and that none of the reactants are reformed in any side reactions, the relative rate coefficient, k_{rel} , is given according to the following expression:

$$\ln \left\{ \frac{[P]_0}{[P]_t} \right\} = k_{\text{rel}} \ln \left\{ \frac{[I]_0}{[I]_t} \right\}; k_{\text{rel}} = \frac{k_p}{k_i} \quad (1)$$

where [P]₀, [I]₀, [P]_t, and [I]_t are concentrations of the parent and the isotopologue at the start and at the time *t*, respectively, and k_p and k_i are the corresponding rate coefficients. A plot of $\ln\{[P]_0/[P]_t\}$ vs $\ln\{[I]_0/[I]_t\}$ will thus give the relative reaction rate coefficient $k_{\text{rel}} = k_p/k_i$ as the slope.

Control experiments were performed to check for loss of fluoromethane via photolysis, dark chemistry, and heterogeneous reactions in the reactor. The lifetime of fluoromethane in the reaction chamber was investigated with purified air as diluent and with the relevant radical precursor mixtures in purified air in experiments lasting from 8 to 15 h. The photostability of fluoromethane toward the radiation used in generating the radicals (see below) was studied in a separate experiment with purified air as diluent: no direct photolysis in the reactor was detected.

The experimental FTIR spectra were analyzed using a global nonlinear least-squares spectral fitting procedure.⁴¹ In this method, the spectrum of the mixture of absorbing species is first simulated by calculation from initial estimates of the absorber concentrations. The calculation is then iterated to minimize the residual between the measured and simulated spectrum using the Levenberg–Marquardt algorithm to adjust the absorber concentrations, continuum level, and instrument line shape parameters. The absorption coefficients are normally calculated from the HITRAN database.⁴² When HITRAN line parameter data are not available, high-resolution FTIR spectra are used to approximate the absorption coefficients.

The spectral features used in the analyses were the C–H and C–D stretching bands in the 3150–2700 and 2300–1900 cm⁻¹ regions, respectively. The spectral data for HCl, H₂O, HDO,

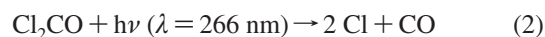
CO, CO₂, O₃, and CH₄ were taken from the HITRAN database. For CH₃F, ¹³CH₃F, CD₃F, HC(O)F, DC(O)F, DCl, and the overtone/combinations bands of O₃ in the 3100–2700 cm⁻¹ range (for which HITRAN does not yet provide all isotopic data), experimental FTIR spectra obtained in our laboratory were used. The infrared spectrum of a trace impurity in the ¹³CH₃F sample was identical to one previously obtained from the spectrum of the commercial ¹³CH₃Br sample by carrying out a short photolysis experiment with Cl₂ present. The impurity reacted much faster than ¹³CH₃F and ¹³CH₃Br did and by spectral subtraction employing spectra of the irradiated sample, HCl, and ¹³CH₂O, we obtained a spectrum of the C–H stretching region of what we tentatively suggest is di-¹³C-labeled CH₃OCH₃. Table S1 (Supporting Information) sums up the wavenumber regions employed and the chemical components included in the analyses.

The data from the independent experiments were analyzed according to eq 1 using a weighted least-squares procedure that includes uncertainties in both reactant concentrations.⁴³ The uncertainty in the concentration determination was taken as 1% of the initial concentration.

2.2. LFP–RF Experimental Technique. The laser flash photolysis (LFP)–resonance fluorescence (RF) technique was employed in a series of experiments to measure temperature-dependent rate coefficients for the reaction of Cl atoms with CH₃F in N₂ bath gas. The LFP–RF apparatus was similar to those employed in several previous studies of chlorine atom kinetics carried out at Georgia Tech.^{44–49} A schematic diagram of the apparatus is published elsewhere.⁵⁰ Important features of the apparatus as well as experimental details that are specific to this study are summarized below.

Two different reaction cells were employed in the LFP–RF study. All experiments at $T \leq 428$ K employed a jacketed Pyrex reaction cell⁵⁰ with an internal volume of ~ 160 cm³. The cell was maintained at a constant temperature by circulating ethylene glycol (for $428 \text{ K} \geq T \geq 300 \text{ K}$) or a 2:1 ethanol–methanol mixture (for $T \leq 276 \text{ K}$) from thermostated baths through the outer jacket. All experiments at $T > 428$ K employed a quartz reaction cell with an internal volume of ~ 250 cm³. This cell was maintained at a constant temperature by passing current through high-resistance-wire heaters that were wrapped around it. Copper–constantan (for low temperature studies) or chromel–alumel (for high temperature studies) thermocouples could be inserted into the reaction zone through a vacuum seal, thus allowing measurement of the gas temperature in the reaction volume (i.e., the volume from which fluorescence could be detected) under the precise pressure and flow rate conditions of the experiment. Temperature variation within the reaction volumes of these cells have been found to be <0.5 K at $T = 270$ K and <1.5 K at $T = 570$ K.

Chlorine atoms were produced by 266 nm laser flash photolysis of phosgene:



Fourth harmonic radiation from a Quanta Ray model DCR-2A Nd:YAG laser served as the 266 nm light source; the pulse width was ~ 6 ns and fluences employed in this study ranged from 1.2 to 10 mJ cm⁻² pulse⁻¹.

An atomic resonance lamp situated perpendicular to the photolysis laser excited resonance fluorescence in the photolytically generated chlorine atoms. The resonance lamp consisted of an electrodeless microwave discharge through about 1 Torr of a flowing mixture containing a trace of Cl₂ in helium. Radiation was coupled out of the lamp through a magnesium

fluoride window and into the reaction cell through a magnesium fluoride lens. Before entering the reaction cell, the lamp output passed through a flowing gas filter containing 3 Torr cm of N₂O in N₂; this filter blocked virtually all O atom impurity emissions at 130–131 nm while transmitting the Cl atom emissions in the 135–140 nm wavelength range. Fluorescence was collected by a magnesium fluoride lens on an axis orthogonal to both the photolysis beam and the resonance lamp beam and was imaged onto the photocathode of a solar blind photomultiplier. The region between the reaction cell and the photomultiplier was purged with N₂; in addition, a calcium fluoride window was inserted into this region to prevent detection of lamp emissions at wavelengths shorter than 125 nm (Lyman- α H atom emission, for example). Fluorescence intensities were found to vary linearly with atom concentration up to levels several times higher than any used in the kinetics experiments ($[\text{Cl}]_0 \leq 4 \times 10^{11}$ atoms cm⁻³ in all experiments). Signals were processed using photon-counting techniques in conjunction with multichannel scaling. For each chlorine atom decay measured, signals from a large number of laser shots were averaged to obtain a well-defined temporal profile over (typically) a factor of 30 variation in the Cl atom concentration. The multichannel scalar sweep was triggered prior to the photolysis laser in order to allow a pretrigger baseline to be obtained.

In order to avoid accumulation of photochemically generated reactive species, all experiments were carried out under “slow flow” conditions. The linear flow rate through the reactor was in the range of 2.0–3.1 cm s⁻¹, while the laser repetition rate was varied over the range of 2–10 Hz (it was 5 Hz in most experiments). Since the direction of flow was perpendicular to the photolysis laser beam, no volume element of the reaction mixture was subjected to more than a few laser shots. Phosgene and CH₃F were flowed into the reaction cell from 12-L Pyrex bulbs containing dilute mixtures in N₂, while N₂ was flowed directly from its high-pressure storage tank. The partial pressure of each component in the reaction mixture was evaluated from mass flow rate and total pressure measurements. The fractional concentration of the CH₃F in the CH₃F/N₂ mixture was periodically determined via UV photometry at 184.9 nm using a Hg pen-ray lamp as the light source and a 1/4 m monochromator to isolate the 184.9 nm Hg line. The molecular absorption cross-section for CH₃F at 184.9 nm was measured during this study and determined to be $(4.9 \pm 0.4) \times 10^{-21}$ cm², where the uncertainty represents an estimated accuracy at the 95% confidence level.

The pure gases used in this study had the following stated minimum purities: N₂, 99.999%; Cl₂CO, 99.0%; CH₃F, 99.0%; for Cl₂CO and CH₃F, the stated purities refer to the liquid phase in the high-pressure storage cylinders. Nitrogen was used as supplied, while Cl₂CO and CH₃F were degassed repeatedly at 77 K before use.

2.3. Electronic Structure Calculations. MP2,⁵¹ CCSD(T),⁵² and CBS-QB3^{53,54} calculations were carried out with the Gaussian 03 program.⁵⁵ Unrestricted wave functions were used to describe open shell systems and bond-breaking processes; singlet ground-state structures were calculated using a restricted wave function. Additional RHF-CCSD(T)⁵² coupled cluster geometry optimizations were carried out by employing the Molpro 2002.6 program package,⁵⁶ in which open shell systems are described by the RHF-UCCSD(T) model, whereas closed shell systems are described by the RHF-RCCSD(T) model.^{57–59} The core electrons were kept frozen in the calculations. Dunning’s correlation-consistent aug-cc-pVXZ (X = D, T, Q) basis sets^{60,61} were employed in all calculations. CCSD(T)/aug-

cc-pVTZ//MP2/aug-cc-pVTZ and CCSD(T)/aug-cc-pVQZ//MP2/aug-cc-pVQZ single-point correlation energies were extrapolated toward the basis-set limit using the extrapolation scheme of Halkier et al.⁶²

$$E_{XY}^{\infty} = \frac{X^3 E_X - Y^3 E_Y}{X^3 - Y^3} \quad (3)$$

where E_X is the correlation energy obtained with the highest cardinal number X , and E_Y is the correlation energy obtained with cardinal number Y equal to $X - 1$ (the cardinal numbers of the aug-cc-pVTZ and aug-cc-pVQZ basis sets are 3 and 4, respectively). In the following, such extrapolations will be denoted CCSD(T)/EB₄₃ with “EB” being short for extrapolated basis.

The minimum energy path (MEP) connecting reactants and products were computed at the MP2/aug-cc-pVXZ (X = D, T) level of theory using the intrinsic reaction coordinate (IRC) method of Gonzales and Schlegel.⁶³ The IRC calculations were carried out in mass-weighted Cartesian coordinates using a step size of 0.02 u^{1/2} bohr.

2.4. Calculations of Rate Coefficients. Calculations of rate coefficients were carried out using interpolated variational transition state theory by mapping (IVTST-M)⁶⁴ using the sparse grid of geometries, gradients, and Hessians from the ab initio IRC calculations as input. The MEP was followed in mass-scaled (scaling mass equal to 1 u) curvilinear coordinates using the RODS algorithm.⁶⁵ In both reactions a step size of 0.002 bohr was used. The electronic energy of the MEP was corrected by the interpolated single-point energy method (ISPE)⁶⁶ using the extrapolated CCSD(T) energies computed at all stationary points as input. In a second procedure, the interpolated optimized energies (IOE) method,⁶⁷ in which the extrapolated CCSD(T) energies and scaled frequencies at the stationary points were used, was applied to the reaction of CH₃F with chlorine. The electronic energies of the MEP were corrected by the SECKART method, in which a single Eckart potential is fitted to the differences between the higher level CCSD(T)/EB₄₃/MP2/aug-cc-pVXZ (X = T, Q) and the lower level MP2/aug-cc-pVTZ energies at all stationary points. The frequencies were corrected by the ICL method (interpolated corrections based on the logarithm of ratios). From this information the ground-state vibrationally adiabatic potential curve, V_a^G , was obtained.

The POLYRATE program⁶⁸ was used to calculate the rate coefficients over the temperature range of 200–1000 K using improved canonical variational theory (ICVT)⁶⁹ for the chlorine reaction and canonical variational theory (CVT)⁷⁰ for the OH reaction. Semiclassical tunneling corrections have been included using the centrifugal-dominant small-curvature adiabatic ground-state tunneling (called small-curvature tunneling or SCT) approximation.⁷¹ The transmission coefficient also includes the classical adiabatic ground-state (CAG) transmission coefficient,⁷² which adjusts the quantal corrections for the difference between V_a^G at its maximum and at the CVT transition state. The calculations of the kinetic isotope effects were based on a single reaction path using the methods outlined in refs 65 and 73.

In the chlorine reaction, the two spin-orbit states ²P_{3/2} (lowest) and ²P_{1/2} of Cl having degeneracies of 4 and 2, respectively, and separated by 882 cm⁻¹ were included in the calculation of the electronic partition function. Similarly, in the OH reaction the ²Π_{3/2} and ²Π_{1/2} spin-orbit states of the OH radical were included; both having degeneracy equal to 2 and separated by 140 cm⁻¹. To estimate the contribution of SO (spin-orbit) coupling to the potential energy surfaces of reactions, SO matrix elements were calculated for the stationary

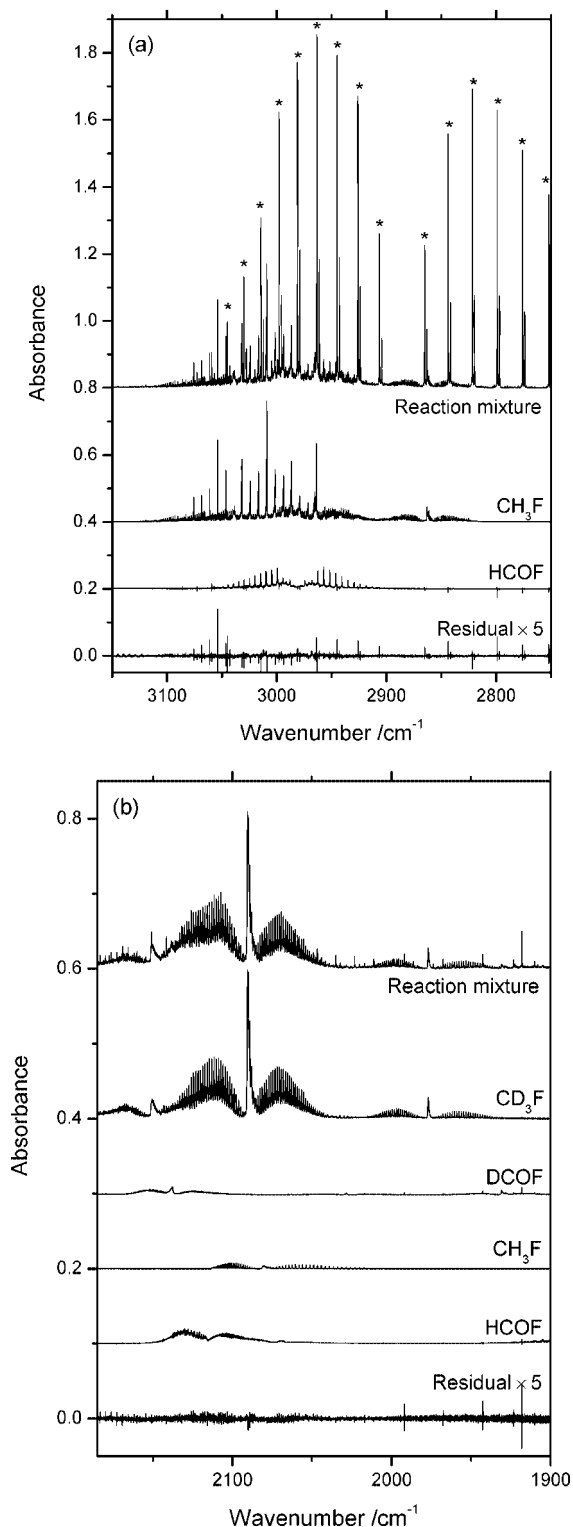


Figure 1. Experimental FTIR spectra of CH₃F/CD₃F/Cl₂ reaction mixtures after 12 min photolysis and of the major chemical components retrieved by spectral fitting. (a) Spectrum of the CH-stretching region 3150–2750 cm⁻¹. Bands marked with * are due to HCl. Compounds included in the spectral analysis: CH₃F, HCOF, H₂O, HDO, and HCl. (b) Spectrum of the CD-stretching region 2185–1900 cm⁻¹. Compounds included in the spectral analysis: CH₃F, CD₃F, HCOF, DCOF, H₂O, CO, and DCl.

points obtained at the MP2/aug-cc-pVTZ level of theory using the Breit–Pauli Hamiltonian as implemented in the Molpro 2002.6 program package.⁷⁴ Wave functions for the SO states were generated using MRCI with reference CASSCF configurations only and the 6-311++G(3df, p) basis set.

The vibrational–rotational partition functions were assumed to be separable and the rotational partition functions were approximated by their classical limit. The vibrational partition functions were calculated within the harmonic oscillator approximation for all modes, except for the C···H···OH torsional mode in the transition state of CH₃F + OH, which was handled by the hindered rotor RW scheme.⁷⁵ The potential of the torsional mode, $V(\phi)$, was calculated at the MP2/aug-cc-pVTZ level of theory and fitted to $V(\phi) = \frac{1}{2}W(1 - \cos \phi)$; the barrier height was found to be $W = 454$ cm⁻¹. For the reaction of CH₃F with chlorine, all frequencies were scaled in the calculation based on the MP2/aug-cc-pVTZ MEP. The scaling factor $c = 0.9552$ applied to the frequencies was calculated according to⁷⁶

$$c = \sum (\tilde{\nu}_i^{\text{exp}} \tilde{\nu}_i^{\text{theo}}) / \sum (\tilde{\nu}_i^{\text{theo}})^2 \quad (4)$$

where $\tilde{\nu}_i^{\text{exp}}$ are the experimental frequencies of vibration, and $\tilde{\nu}_i^{\text{theo}}$ are the theoretically calculated frequencies of vibration for the modes of CH₃F, CH₂F, and HCl.

3. Results and Discussion

3.1. Experimental Study. 3.1.1. Relative Rate Experiments.

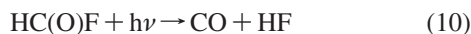
The kinetic isotope effects were determined in relative rate experiments carried out under low NO_x conditions (NO_x < 100 ppbv). According to a previous mechanistic study,²⁴ the Cl (and presumably also the OH) initiated oxidation of CH₃F will, under the present reaction conditions, essentially proceed via reactions 5–9:



Wallington et al.²⁴ found that reaction 7 proceeds predominantly, if not exclusively, via reaction 7a. Further, reaction 9a is much slower than the reaction of other alkyl peroxy radicals with HO₂ and they only observed a spectral feature around 3650 cm⁻¹, which was tentatively attributed to CH₂FOOH, in experiments with initial CH₃F concentrations around 100 ppm. In addition, a later mechanistic study of the gas phase reaction of CH₂FO₂ radicals with HO₂ shows that reaction 9a dominates over reaction 9b.⁷⁷

During the reaction of Cl atoms with fluoromethane, OH radicals will eventually be generated from the HO₂ radicals and thereby influence the kinetics. We therefore modeled the degradation reactions of CH₃F in the static reactor using FACSIMILE⁷⁸ to find the optimum starting conditions. The basic model of our reactor consists of around 200 equations describing O_x, HO_x, NO_x, FO_x, ClO_x, BrO_x, and CH₄ related “background” reactions in the chamber;⁷⁹ the rate coefficient data have been taken from the latest JPL²⁵ and IUPAC⁸⁰ kinetic data evaluations (the photolysis rates of photolabile constituents were determined experimentally in our laboratory). In addition, we included the reactions describing the Cl- and OH-initiated oxidation of CH₃F as indicated by reactions 5–9 and the subsequent degradation reactions of HC(O)F.^{81–83} Using 5 ppm CH₃F and 10–20 ppm Cl₂ as starting conditions, the model indicated that the loss of CH₃F due to reactions with OH radicals

in the Cl atom experiments was less than 1% of the total loss. The model also predicted that the concentration of HC(O)F formed could become as high as 0.5 ppm; the absorption lines of this molecule could therefore interfere with the analyses of the C–H and C–D stretching regions of the spectrum. To prevent/reduce such a buildup, we employed the Philips TUV 30W lamp with $\lambda_{\max} \sim 254$ nm, which will photolyze HC(O)F:



Examples of the FTIR spectra obtained from the kinetic studies of the CH₃F/CD₃F reaction with Cl atoms and the resulting residuals from the nonlinear least-squares spectral analyses are shown in Figure 1. Spectra from the CH₃F/¹³CH₃F + Cl experiments are shown in Figure S1 (Supporting Information). The decays of CH₃F, ¹³CH₃F, and CD₃F in the presence of Cl atoms are shown as plots of $\ln\{[\text{CH}_3\text{F}]_0/[\text{CH}_3\text{F}]_t\}$ vs $\ln\{[^{13}\text{CH}_3\text{F}]_0/[^{13}\text{CH}_3\text{F}]_t\}$ and $\ln\{[\text{CH}_3\text{F}]_0/[\text{CH}_3\text{F}]_t\}$ vs $\ln\{[\text{CD}_3\text{F}]_0/[\text{CD}_3\text{F}]_t\}$ in Figure 2a,b. Least-squares fitting of the data resulted in the following kinetic isotope effects: $k_{\text{Cl}+\text{CH}_3\text{F}}/k_{\text{Cl}+^{13}\text{CH}_3\text{F}} = 1.016 \pm 0.006$ and $k_{\text{Cl}+\text{CH}_3\text{F}}/k_{\text{Cl}+\text{CD}_3\text{F}} = 5.11 \pm 0.07$. The uncertainties represent 2σ from the least-squares analysis and refer to precision only.

Figures S2 and S3 (Supporting Information) show experimental FTIR spectra of the reaction mixtures CH₃F/¹³CH₃F/O₃/H₂ and CH₃F/CD₃F/O₃/H₂, respectively. The ozone band at 3046 cm⁻¹ ($3\nu_3$) partly obscures the perpendicular band of CH₃F ($\nu_4(\text{E})$) and overlaps the parallel band of CH₃F ($\nu_1(\text{E})$). This complicated the spectral analysis substantially. The relative concentrations of CD₃F during the reactions were determined from spectral analysis of the C–D stretching region (2230–2150 cm⁻¹), as this region is not obscured significantly by the CO₂ fundamental (ν_3) and the $2\nu_1/3\nu_2$ ozone bands. From the decay data of the fluoromethane isotopologues in the presence of OH radicals, shown in the form of $\ln\{[\text{CH}_3\text{F}]_0/[\text{CH}_3\text{F}]_t\}$ vs $\ln\{[^{13}\text{CH}_3\text{F}]_0/[^{13}\text{CH}_3\text{F}]_t\}$ and $\ln\{[\text{CH}_3\text{F}]_0/[\text{CH}_3\text{F}]_t\}$ vs $\ln\{[\text{CD}_3\text{F}]_0/[\text{CD}_3\text{F}]_t\}$ in Figure 2c,d, the following kinetic isotope effects were extracted: $k_{\text{OH}+\text{CH}_3\text{F}}/k_{\text{OH}+^{13}\text{CH}_3\text{CH}_3\text{F}} = 1.067 \pm 0.006$ and $k_{\text{OH}+\text{CH}_3\text{F}}/k_{\text{OH}+\text{CD}_3\text{F}} = 4.067 \pm 0.018$. Again, the uncertainties represent 2σ from the least-squares analysis and refer to precision only.

The “natural” removal of CH₃F from the gas phase (purified air) in the reactor is shown in Figure S4 (Supporting Information). Assuming the (small) decay to be first-order in CH₃F, the natural loss rate coefficient was determined to be 4×10^{-8}

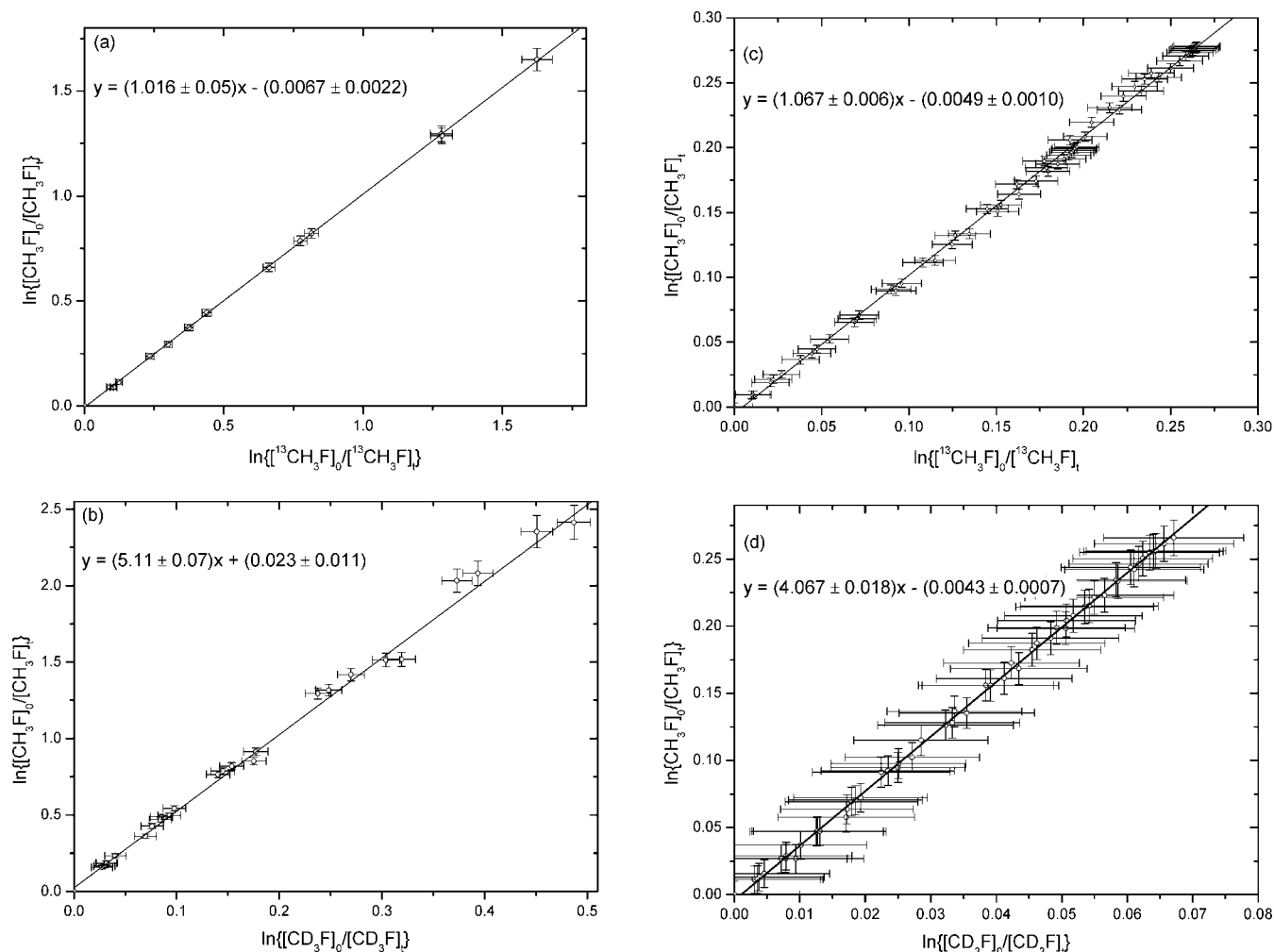


Figure 2. Relative rate plots showing the decays of CH₃F, ¹³CH₃F, and CD₃F at 1013 hPa and 298 K in the presence of Cl atoms and OH radicals. The slopes correspond to the relative reaction rate $\alpha = k_{\text{light}}/k_{\text{heavy}}$; the errors on the slopes correspond to 2σ from the statistical analyses and do not include possible systematic errors. Error bars assigned to the individual data points correspond to either 1% of the starting concentration or the 1σ error in the spectral fitting procedure, whichever is largest. (a) Decay of CH₃F vs ¹³CH₃F in the presence of Cl atoms; $\alpha = 1.016 \pm 0.006$ (determined from 14 data points from three independent experiments). (b) Decay of CH₃F vs CD₃F in the presence of Cl atoms; $\alpha = 5.11 \pm 0.07$ (26 data points from four independent experiments). (c) Decay of CH₃F vs ¹³CH₃F in the presence of OH radicals; $\alpha = 1.067 \pm 0.006$ (56 data points from three independent experiments). (d) Decay of CH₃F vs CD₃F in the presence of OH radicals; $\alpha = 4.067 \pm 0.018$ (55 data points from five independent experiments).

s⁻¹ (lifetime ~ 240 days). For a realistic reaction mixture in the OH radical experiments, CH₃F/H₂O₃ 5:2000:200 ppm in purified air, the loss rate coefficients of CH₃F and O₃ were simultaneously determined to be 5.6 × 10⁻⁷ and 1 × 10⁻⁶ s⁻¹, respectively. The lifetime of CH₃F in the reaction chamber under these conditions thus decreases to around 20 days. Assuming the difference between the two CH₃F loss rates to be due to gas-phase reaction with O₃ places an upper limit of $k_{O_3+CH_3F} < 10^{-22}$ cm³ molecule⁻¹ s⁻¹. The kinetic analysis according to eq. 1 assumes that only one loss process is taking place: other loss processes, such as gas-phase or surface reactions with the radical precursors and natural wall loss, will give rise to systematic errors in the kinetic isotope effects, especially in the OH reaction, which is slow. The OH experiments generally lasted for 3–4 h, including spectral recording and waiting time between the photolysis, during which around 15% of the initial fluoromethane reacted. Taking the rate coefficient for the OH reaction with fluoromethane as 2.1 × 10⁻¹⁴ cm³ molecule⁻¹ s⁻¹ at 298 K,²⁵ a rough estimate of the average OH concentration during the entire experiment (including waiting periods and time for spectrum recording) is 5 × 10⁸ molecules cm⁻³, which gives a ratio >20 between the loss due to reaction with OH radicals and the “dark” loss of fluoromethane. Taking the numbers given above, a numerical simulation shows that the systematic error in $k_{OH+CH_3F}/k_{OH+CD_3F}$ is estimated to be -0.014. For $k_{OH+CH_3F}/k_{OH+^{13}CH_3F}$, the corresponding systematic error is estimated to be even smaller. That is, the known systematic errors in the OH radical experiments due to dark reactions of fluoromethane result in apparent KIEs that are too small, but only by the same amount as the 2σ statistical error of the data analysis. For a realistic reaction mixture in the Cl atom experiments, CH₃F/Cl₂ 5:20 ppm in purified air, the loss rate coefficient of CH₃F was determined to be 3.7 × 10⁻⁷ s⁻¹ (lifetime ~ 31 days). The Cl atom experiments generally also lasted 3–4 h; the conversion of the fluoromethanes, however, was around 30%. The recommended value of the CH₃F reaction rate coefficient with Cl atoms at 298 K is 3.5 × 10⁻¹³ cm³ molecule⁻¹ s⁻¹ at 298 K,²⁵ which places the average Cl atom concentration during the entire experiment around 6 × 10⁷ atoms cm⁻³, which gives a ratio >60 between the loss due to reaction with Cl atoms and the dark loss of fluoromethane. The dark reactions will therefore not constitute an important systematic error in this system.

Experimental kinetic isotope effects for the Cl and OH reactions of CH₄, CH₃Cl, and CH₃F are summarized in Table 1. The ¹²C/¹³C KIEs in the Cl and OH reactions of CH₃OH recently determined by Feilberg et al.¹² have been included for comparison. As can be seen, the ¹²C/¹³C KIE in the Cl reaction with CH₃OH is of similar magnitude as in CH₃Cl, CH₄, and CH₃F; for the OH reaction, the ¹²CH₃OH/¹³CH₃OH and ¹²CH₃Cl/¹³CH₃Cl KIEs are of similar magnitude as for CH₃F but, again, an order of magnitude larger than for CH₄.

3.1.2. LFP–RF Results. Photodissociation of Cl₂CO at λ ≈ 235 nm has been shown to be a concerted process; i.e., both chlorine atoms are produced on a time scale that is short compared to a rotational period.⁸⁴ The fraction of chlorine atoms generated in the spin–orbit excited state, Cl(²P_{1/2}), is thought to be significant.⁸⁵ Rate coefficients for the relaxation of Cl(²P_{1/2}) in equilibrium with Cl(²P_{3/2}) are reported in the literature for each of the components (N₂, Cl₂CO, CH₃F) of the experimental gas mixtures;⁸⁵ given the values of those quenching rate coefficients, it can be safely assumed that all Cl + CH₃F kinetic data reported in this study are representative of an equilibrium mixture of Cl(²P_{1/2}) and ground-state Cl(²P_{3/2}) atoms.

TABLE 1: Experimental ¹³C and ²H (D) Kinetic Isotope Effects, α = k_{light}/k_{heavy} , in the Reactions of CH₃F, CH₃Cl, CH₄, and CH₃OH with Cl Atoms and OH Radicals at 298 K

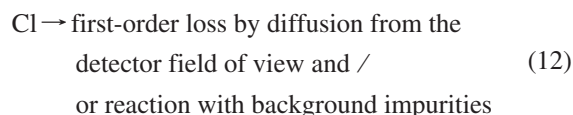
isotopologues	kinetic isotope effect	
	Cl reaction	OH reaction
¹² CH ₃ F/ ¹³ CH ₃ F	1.016 ± 0.006 ^a	1.067 ± 0.006 ^a
CH ₃ F/CD ₃ F	5.11 ± 0.07 ^a	4.067 ± 0.018 ^a
¹² CH ₃ Cl/ ¹³ CH ₃ Cl	1.070 ± 0.010 ⁸	1.059 ± 0.008 ⁸
CH ₃ Cl/CD ₃ Cl	4.91 ± 0.07 ⁸	3.9 ± 0.4 ⁸
¹² CH ₄ / ¹³ CH ₄	1.058 ± 0.002 ³	1.0039 ± 0.0004 ²
CH ₄ /CHD ₃	4.73 ± 0.04 ³	3.30 ± 0.50 ¹
¹² CH ₃ OH/ ¹³ CH ₃ OH	1.055 ± 0.016 ¹²	1.031 ± 0.020 ¹²
CH ₃ OH/CD ₃ OH	3.011 ± 0.059 ¹²	2.57 ± 0.11 ¹²

^a This work.

All experiments were carried out under pseudo-first-order conditions with CH₃F in large excess over Cl atoms. Hence, in the absence of side reactions that remove or produce Cl atoms, the Cl atom temporal profile following the laser flash would be described by the relationship

$$\ln\{[Cl]_0/[Cl]_t\} = (k_{Cl+CH_3F}[CH_3F] + k_{12})t = k't \quad (11)$$

where k_{12} is the rate coefficient for the reaction



The bimolecular rate coefficients of interest, $k_{Cl+CH_3F}(p,T)$, are determined from the slopes of k' vs [CH₃F] plots for data obtained at constant T and p . Observation of Cl temporal profiles that are exponential, i.e., obey eq 11, a linear dependence of k' on [CH₃F], and invariance of k' to variation in laser photon fluence and photolyte (i.e., phosgene) concentration, strongly suggests that reactions 5 and 12 are, indeed, the only processes that significantly influence the Cl time history.

Typical data are shown in Figures 3 and 4, and measured bimolecular rate coefficients, $k_{Cl+CH_3F}(p,T)$, along with relevant experimental conditions, are summarized in Table 2. The results from Table 2 are shown in the form of an Arrhenius plot in Figure 5. The dashed line in Figure 5 is a fit to the data using the modified Arrhenius expression:

$$k_{Cl+CH_3F}(T) = A \times (T/298)^n \exp\{-(E_a/RT)\} \quad (13)$$

A nonlinear least-squares analysis leads to the following best-fit parameters: $A = 1.14 \times 10^{-12}$ cm³ molecule⁻¹ s⁻¹, $n = 2.26$, and $E_a/R = 313$ K.

As can be seen in Table 2 and Figure 5, the random errors encountered in the determination of a rate coefficient at a given temperature and pressure are relatively small. Reactive impurities contained in the CH₃F could be a possible source of systematic error and, in part, could be an explanation for the non-Arrhenius temperature behavior of $k_{Cl+CH_3F}(T)$ observed in this study. In a previous study of this reaction, Manning and Kurylo^{20,25} reported an analysis of a CH₃F sample from the same supplier as used in the present study. Methane and C₂H₅F were found at levels of 10 and 35 ppm, respectively. Using these concentrations and the evaluated literature values²⁵ for the temperature-dependent rate coefficients for the reaction of Cl atoms with each of the above impurities, it can be concluded that neither impurity reaction made a significant contribution to our reported values for $k_{Cl+CH_3F}(T)$. It is worth noting that the study of Manning and Kurylo²⁰ was carried out using a

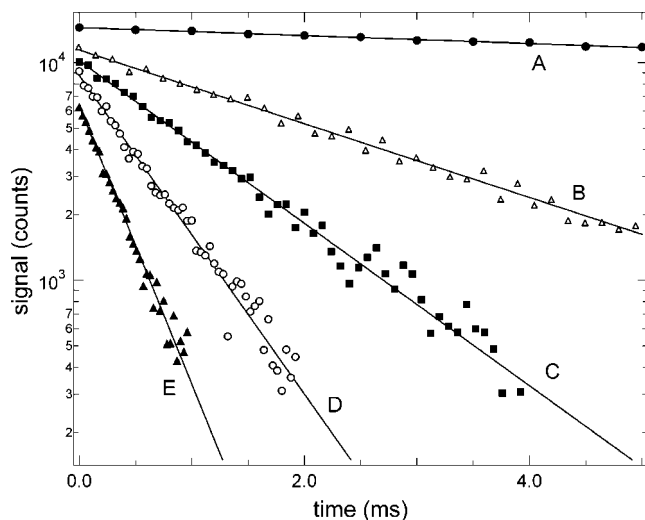


Figure 3. Typical Cl atom temporal profiles observed at $T = 298$ K in 133 hPa of N_2 . Experimental conditions: $[Cl_2CO] = 7.4 \times 10^{14}$ molecules cm^{-3} ; $[Cl]_0 = 3.5 \times 10^{11}$ atoms cm^{-3} ; $[CH_3F]$ in units of 10^{15} molecules $cm^{-3} =$ (A) 0, (B) 0.839, (C) 2.12, (D) 4.08, and (E) 7.57. The lines are obtained from linear least-squares analyses of the data; their slopes give the following pseudo-first-order decay rates in units of s^{-1} : (A) 54, (B) 400, (C) 869, (D) 1650, and (E) 2930. For the sake of clarity, traces B, C, D, and E are scaled by factors of 2, 1.75, 2, and 0.75, respectively.

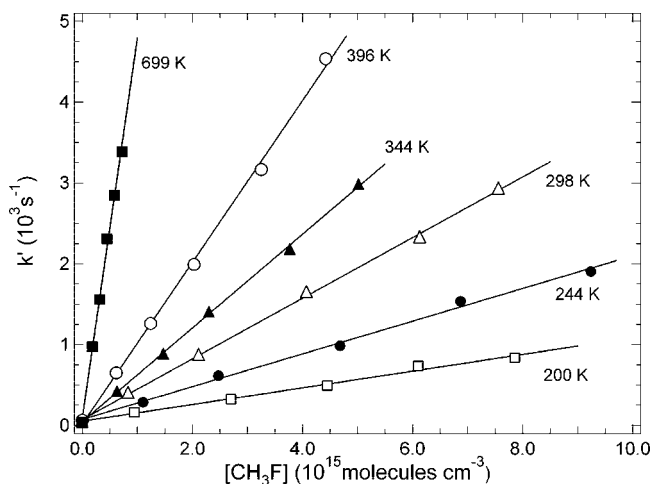


Figure 4. Plots of k' , the pseudo-first-order Cl atom decay rate, vs $[CH_3F]$ over a range of temperatures. All data shown were obtained at a total pressure of 133 hPa. The solid lines are obtained from linear least-squares analyses, and the resulting bimolecular rate coefficients, i.e., the slopes of the plots, are listed in Table 2.

technique very similar to the LFP–RF portion of this study, although over a much smaller temperature range (216–296 K), and that their results are almost identical with those reported in this study. Taking into account the small amount of random errors, the possibility of unidentified impurities (unlikely to be important based on the above discussion) and other systematic errors such as the determination of the temperature and of the concentration of the reactant, we estimate that the overall accuracy of our measured values of $k_{Cl+CH_3F}(T)$ is $\pm 20\%$ (95% confidence level) over the entire temperature range of the LFP–RF study.

3.2. Computational Study. 3.2.1. Structures and Energetics of Stationary Points. The minimum energy path (MEP) connecting reactants and products of the Cl and OH reaction with CH_3F was computed using the intrinsic reaction coordinate (IRC) method⁶³ at the MP2/aug-cc-pVXZ ($X = D, T$) levels of

theory. In addition to the saddle point of the hydrogen abstraction reaction, we have located a prereaction van der Waals adduct on the MEP for both reactions. On the product side of the MEP there is a postreaction van der Waals adduct between CH_2F and HCl. These adducts have also been reported in previous theoretical studies.^{28,33,34} We were not able to reproduce the postreaction adduct of the OH reaction with CH_3F , which is reported by El-Taher³³ at the UHF/6-31G(d) level of theory.

The stationary points on the MEP of the Cl and OH reactions with CH_3F were optimized at several levels of theory: MP2/aug-cc-pVXZ ($X = D, T, Q$) and CCSD(T)/aug-cc-pVDZ. The structures of the stationary points of the Cl reaction with CH_3F are given in Figure S5 (Supporting Information), while the structural parameters obtained at the different levels of theory are listed in Table S2 (Supporting Information). Structures and structural parameters for the stationary points of the OH reaction are given in Figure S6 and Table S3 (Supporting Information), respectively. The structural results indicate that the aug-cc-pVTZ basis set provides a reasonable description of the stationary points when compared to the larger aug-cc-pVQZ basis set; the largest difference is 2.4 pm for the C–F bond in CH_2F , which is within what is expected for the two levels.⁸⁶ The structures of the stationary points were also optimized at the CCSD(T)/aug-cc-pVDZ level of theory to test the quality of the MP2 model, the CCSD(T) model being more robust.⁸⁶ For the reaction of OH with CH_3F , the structures predicted by the MP2/aug-cc-pVQZ and CCSD(T)/aug-cc-pVDZ model show only minor differences (see Table S3, Supporting Information), the largest difference concerning the C–H(4) bond (3.4 pm) of the saddle point, leading to a slightly more product-like structure of the saddle point in the CCSD(T) model compared to the MP2 model. The differences between the two models are more pronounced for the Cl reaction with CH_3F . As can be seen from Table S2 and Figure S5 (Supporting Information), the CCSD(T) model predicts the saddle point of the system to be much more product-like than what is predicted by the MP2 model. It is difficult to estimate the full effect of this as CCSD(T) calculations currently are too time-consuming to offer a realistic alternative in computations of the potential energy surfaces (PES) of the reactions investigated in this work. When comparing the structural results for CH_3F and OH as well as the reaction products CH_2F , HCl, and H_2O with the experimental values (Table S2 and S3, Supporting Information), it is seen that all bond lengths are calculated within a range of less than ± 3.0 pm from the experimental values for the MP2/aug-cc-pVXZ ($X = T, Q$) and CCSD(T)/aug-cc-pVDZ levels of theory, in agreement with the established error margins.⁸⁷ The bond angles of CH_3F and H_2O are described in close agreement with experimental data (largest deviation -0.5°); the bond angle of the CH_2F radical deviates around -2.5° in the MP2 and CCSD(T) calculations. The applied levels of theory thus provide reasonable descriptions of the reactants and products.

The energetics of the stationary points involved in the Cl and OH reactions of CH_3F are summarized in Table 3 and 4 and compared to previous results in Tables S4 and S5 (Supporting Information), respectively. The agreement with literature data is generally good. The difference between the CCSD(T)/aug-cc-pVQZ/MP2/aug-cc-pVQZ and the CCSD(T)/EB43/MP2/aug-cc-pVXZ ($X = T, Q$) energies are less than 2 kJ mol^{-1} for both reactions, indicating that the results are close to the basis set limit of the respective level of theory. The calculated enthalpies of reaction for the OH and Cl reactions of CH_3F are in reasonable agreement with the experimental values. The

TABLE 2: Results of the LFP–RF Study of the Reaction of Cl Atoms with CH₃F

T/K	p/hPa	no. of expt ^a	[CH ₃ F] _{max} /10 ¹⁵ cm ⁻³	[Cl ₂ CO]/10 ¹⁴ cm ⁻³	[Cl] ₀ /10 ¹¹ cm ⁻³	fluence/mJ cm ⁻²	k _{max} /s ⁻¹	(k ± 2σ) ^b /10 ¹³ cm ³ s ⁻¹
200	133	6	7.86	10	1.5	2.5	835	1.03 ± 0.08
221	133	6	11.7	10	0.7–1.5	1.2–2.4	1698	1.40 ± 0.02
232	133	6	9.29	9.6	1.2	2.1	1538	1.63 ± 0.14
244	133	6	9.24	9.3	1.1	2.0	1905	2.02 ± 0.13
264	133	6	8.40	9.0	0.8–1.3	1.5–2.4	2324	2.64 ± 0.16
276	133	6	6.39	7.7	1	2.1	2149	3.26 ± 0.09
298	73	6	2.69	6.4	2.5	6.8	1060	3.85 ± 0.10
298	133	6	4.85	6.3	1	2.6	1841	3.53 ± 0.34
298	133	11	5.03	7.0	0.7–2.5	1.6–6.6	2047	3.73 ± 0.21
298	133	6	7.57	7.4	3.5	7.4	2929	3.75 ± 0.11
320	133	6	3.86	7.2–14	1.1	1.2–2.5	2012	5.00 ± 0.33
344	133	6	5.02	6.0	1.3	3.6	2982	5.80 ± 0.14
348	133	5	4.76	6.7	0.9	2.2	2198	6.63 ± 0.22
378	133	6	2.06	5.4	0.6	1.9	2047	9.62 ± 0.19
396	133	6	4.42	5.1	1	3.2	4537	10.0 ± 0.4
426	133	6	4.41	4.9	1.9	6.4	5205	11.5 ± 0.3
428	33	10	3.13	3.2–12	1.8	2.4–10	3969	11.7 ± 0.8
428	133	6	3.81	5.4	0.8	2.5	5270	13.6 ± 0.4
429	133	6	1.47	4.9	0.7	2.2	2281	14.7 ± 1.0
555	133	7	0.815	2.7	0.3–0.5	1.7–3.1	2160	26.2 ± 1.1
699	133	6	0.718	2.7	1.2	7.1	3388	46.9 ± 2.6

^a Experiment defined as measurement of one pseudo-first-order decay rate. ^b Uncertainties represent precision only.

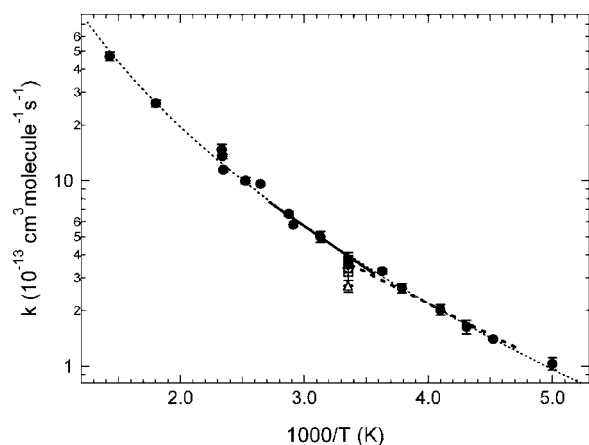


Figure 5. Arrhenius plot for the reaction of Cl atoms with CH₃F: (●) this work (LFP–RF technique), (—) Tschuikow-Roux et al.⁹⁵ using updated temperature-dependent rate coefficients for the Cl + CH₄ reference reaction,²⁵ (–) Manning and Kurylo,²⁰ (□) Wallington et al.,⁴⁴ (○) Tuazon et al.,²³ and (△) Hitsuda et al.²¹ As described in the text, a good fit to our data is obtained using the modified Arrhenius expression $k(T) = 1.14 \times 10^{-12} (T/298)^{2.26} \exp(-313/T) \text{ cm}^3 \text{ molecule}^{-1} \text{ s}^{-1}$ (dotted line).

results obtained at the CCSD(T)/EB₄₃/MP2/aug-cc-pVXZ (X = T, Q) and CBS-QB3 levels of theory are within the uncertainty of experimental values (Table S6, Supporting Information). The experimental values show large uncertainty limits due to the large uncertainties in the heat of formation of CH₃F and CH₂F.

For the loosely bound reaction adducts, one might expect the basis set superposition error (BSSE) to be significant. To estimate the magnitude of this effect, the BSSE in the MP2/aug-cc-pVQZ model of the pre- and postreaction adduct in the chlorine reaction and the prereaction adduct in the OH reaction of CH₃F was approximated by the counterpoise correction.⁸⁸ The BSSE was found to be around 1 kJ mol⁻¹, which we consider negligible in the present context.

3.2.2. Absolute Rate Coefficients. Figure 6a shows the potential energy curve of the minimum energy path, V_{MEP} , and the ground-state vibrationally adiabatic potential energy curve, $\Delta V_{\text{a}}^{\text{G}}$, as a function of the reaction coordinate for the CH₃F +

Cl reaction calculated by the ISPE method using single-point energy corrections from the CCSD(T)/EB₄₃/MP2/aug-cc-pVXZ (X = T, Q) calculations and including the effect of spin–orbit coupling. The generalized normal-mode frequencies of the system as a function of the reaction coordinate are shown in Figure 6b. The curves result from an interpolation of 470 ab initio points with gradients and where the Hessians have been computed at 160 of those points. The $\Delta V_{\text{a}}^{\text{G}}$ curve has two maxima: one at -0.65 bohr (global) and the other at $+0.32$ bohr with a shallow minimum between the two maxima at ca. $+0.19$ bohr. One could assume that two dynamical bottlenecks exist in the reaction system. Recrossing between such two bottlenecks could occur and the assumption of one dividing surface in CVT no longer would be valid. Examination of the situation in the present reaction system shows that, at all temperatures considered, the energy difference between the second-highest maximum and the minimum is less than $k_{\text{B}}T$, k_{B} being the Boltzmann constant. Therefore, recrossing is not expected and the assumption of only a single dividing surface holds.

Figure 7 shows an Arrhenius plot of the calculated rate coefficients for the Cl reaction with CH₃F. For comparison, the figure includes plots of the experimental LFP–RF results of this study and of the recommended rate coefficients,^{25,26} including their uncertainty limits. Since spin–orbit coupling present in the Cl atom becomes smaller during the reaction, it will contribute to the potential energy surface by effectively increasing the barrier height. This was taken into account in the calculation of the rate coefficients. The calculations predict the SO coupling to lower the asymptotic potential energy of the reactants on the MP2/aug-cc-pVTZ MEP by 3.3 kJ mol⁻¹, in good agreement with the a priori assumption of 1/3 of the SO coupling constant of Cl (3.5 kJ mol⁻¹) and previous calculations on similar systems.⁸⁹ For the prereaction adduct, a SO coupling of 1.1 kJ mol⁻¹ was found. At the transition state, the effect of SO coupling is almost quenched (0.1 kJ mol⁻¹). The excited spin–orbit states were only considered in the electronic partition function of the chlorine atom. In the ISPE model, the barrier height was increased by 3.2 kJ mol⁻¹ according to the SO coupling calculated for the MP2/aug-cc-pVTZ geometries. The reaction enthalpy and the energy of the

TABLE 3: Born–Oppenheimer and Zero-Point Corrected Energies (kJ mol⁻¹) of Stationary Points Involved in the Reaction CH₃F + Cl → CH₂F + HCl^a

computational level	ΔE_{RC}	$\Delta(E_{RC}+ZPE)$	ΔE^\ddagger	$\Delta(E^\ddagger+ZPE)$	ΔE_{PC}	$\Delta(E_{PC}+ZPE)$	$\Delta_{rxn}E$	$\Delta_{rxn}(E+ZPE)$
this work ^b								
MP2/aDZ ^c	-8.9	-7.7	29.3	12.1	5.2	-9.2	15.0	-4.8
MP2/aTZ	-8.4	-7.4	24.7	7.8	-1.8	-17.0	7.5	-12.7
MP2/aQZ	-2.9	-1.9	28.2	11.4	0.6	-14.8	9.3	-11.1
MP2/EB ₄₃	0.8	1.8	31.5	14.6	3.4	-12.6	11.6	-8.7
CCSD(T)/aDZ//MP2/aDZ	-9.2	-8.0	28.6	11.4	8.7	-6.5	18.6	-1.2
CCSD(T)/aTZ//MP2/aTZ	-8.6	-7.5	24.7	7.9	3.3	-11.8	12.6	-7.6
CCSD(T)/aQZ//MP2/aQZ	-8.5	-7.5	22.3	5.5	0.2	-15.2	8.6	-11.7
CCSD(T)/EB ₄₃ //MP2/aXZ (X = T, Q)	-8.7	-7.7	21.3	4.5	-1.2	-16.6	6.8	-13.5
CCSD(T)/aDZ	-9.2	-9.2	28.7	10.1	8.6	-7.9	18.5	-1.4

^a ΔE_{RC} is the energy of the prereaction complex, ΔE^\ddagger is the barrier height evaluated at the saddle point, ΔE_{PC} is the energy of the postreaction complex, and $\Delta_{rxn}E$ is the energy of reaction. All energies are relative to that of the reactants. ^b Structures of the stationary points are displayed in Figure S5 (Supporting Information). ^c Abbreviations: aDZ, aug-cc-pVDZ; aTZ, aug-cc-pVTZ; aQZ, aug-cc-pVQZ; EB, extrapolated basis limit (see eq 3 and the following text).

TABLE 4: Born–Oppenheimer and Zero-Point Corrected Energies (kJ mol⁻¹) of Stationary Points Involved in the Reaction CH₃F + OH → CH₂F + H₂O^a

computational level	ΔE_{RC}	$\Delta(E_{RC}+ZPE)$	ΔE^\ddagger	$\Delta(E^\ddagger+ZPE)$	$\Delta_{rxn}E$	$\Delta_{rxn}(E+ZPE)$
this work ^b						
MP2/aDZ ^c	-18.1	-12.1	31.9	25.2	-78.7	-83.1
MP2/aTZ	-12.4	-6.4	35.8	29.4	-78.8	-83.8
MP2/aQZ	-17.1	-11.1	30.3	24.0	-87.5	-92.4
MP2/EB ₄₃	-20.8	-14.8	26.0	19.7	-93.0	-97.9
CCSD(T)/aDZ//MP2/aDZ	-18.5	-12.4	21.7	15.0	-59.6	-64.0
CCSD(T)/aTZ//MP2/aTZ	-18.0	-12.0	20.4	14.0	-65.4	-70.0
CCSD(T)/aQZ//MP2/aQZ	-17.4	-11.4	20.2	13.8	-69.3	-74.2
CCSD(T)/EB ₄₃ //MP2/aXZ (X = T, Q)	-17.2	-11.2	19.7	13.3	-71.3	-76.2
CCSD(T)/aDZ	-16.9	-11.4	21.3	12.5	-59.6	-63.3

^a ΔE_{RC} is the energy of the prereaction complex, ΔE^\ddagger is the Born–Oppenheimer barrier height evaluated at the saddle point, and $\Delta_{rxn}E$ is the Born–Oppenheimer energy of reaction. All energies are relative to that of the reactants. ^b Structures of the stationary points are displayed in Figure S6 (Supporting Information). ^c Abbreviations: aDZ, aug-cc-pVDZ; aTZ, aug-cc-pVTZ; aQZ, aug-cc-pVQZ; EB, extrapolated basis (see eq 3 and the following text).

postreaction adduct were also corrected for the effect of spin–orbit coupling. This method of accounting for SO coupling in dual-level calculations has proved to give reasonable results for other reaction systems.^{89,90} We see that our ICVT/SCT calculation significantly underestimates the rate coefficients for the reaction and does not reproduce the temperature dependence correctly at low temperatures. However, there are some discrepancies in the evaluation of experimental data leading to different recommended rate coefficients and slopes of the Arrhenius plot. Atkinson et al.²⁶ in their evaluation took only the results of Manning and Kurylo²⁰ into account, covering a temperature range of 216–296 K, whereas Sander et al.²⁵ included in their evaluation only the study of Tschuikow-Roux et al.,²² who found a steeper temperature dependence between 273 and 368 K. Atkinson et al. commented in their evaluation that Tschuikow-Roux et al. did not report individual data points but only an Arrhenius expression that meets the other data at 298 K but has a greater temperature dependence in the temperature range above 298 K. Sander et al. in their evaluation slightly modified the results of Tschuikow-Roux et al. based on comparisons of the E_a/R value of the CH₃F + Cl reaction with the Cl and OH reactions with CH₃Cl and CH₃Br. They supposed that the results of Manning and Kurylo are affected by some systematic error at lower temperatures, leading to a less steep slope of the Arrhenius expression. Unfortunately, they do not state the temperature range covered by their recommended values. The results of our LFP–RF study covering a temperature range of 200–700 K show good agreement with both studies, that of Manning and Kurylo in the lower temperature range and that of Tschuikow-Roux et al. in the

higher temperature range. Thus, our results support a nonlinear temperature dependence of the Arrhenius expression over the whole temperature range of 200–700 K. The recommended values of Sander et al. should only be used in the range of approximately 290–370 K. An extrapolation to lower temperatures leads to significantly lower rate coefficients than those measured in our study and those recommended by Atkinson et al. (see Figure 7). The results of our theoretical study as well as that of the theoretical studies of Xiao et al.²⁷ and Rosenman and McKee²⁹ predict a larger temperature dependence in the low-temperature range than was found experimentally in our study and that by Manning and Kurylo.²⁰

There are two reasons for the somewhat short fallen calculated rate coefficients compared with the experimental measurements: First, the vibrational frequencies have been calculated within the harmonic oscillator approximation, which is known to overestimate the true frequencies. Second, the tunneling approximation we have used—the SCT model—underestimates the true tunneling probability. To account for the deficiency in frequencies, a scaling of all modes was applied within the IOE model. The scaling of the frequencies results in almost no changes of the rate constants and the temperature dependence. For the TST model, the calculated rate constants reproduce the experimental values within the uncertainty limits. A comparison to the theoretical work of Xiao and co-workers²⁷ shows the sensitivity of the rate constants to the barrier height. In their rate constants calculations, they applied the ICVT/SCT model based on ab initio calculations of the PES at the QCISD(T)//BH&HLYP level of theory. An electronic barrier height, ΔE^\ddagger , of 20.6 kJ mol⁻¹ results in an underestimation of the rate

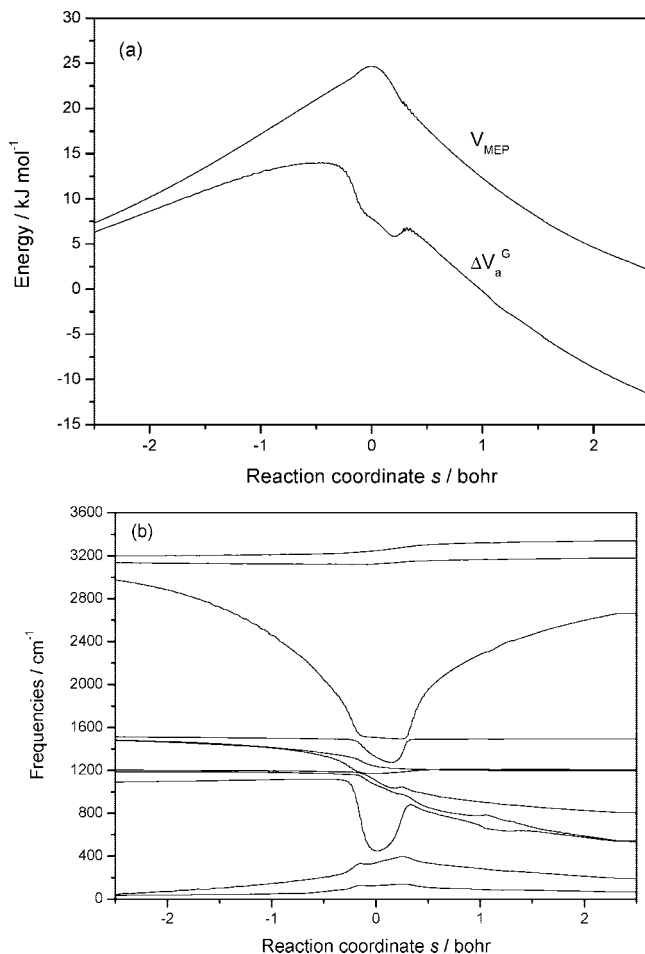


Figure 6. (a) Minimum energy path, V_{MEP} , and vibrationally adiabatic ground-state potential energy curve, ΔV_a^G , as a function of the reaction coordinate, s , for the reaction $\text{CH}_3\text{F} + \text{Cl} \rightarrow \text{CH}_2\text{F} + \text{HCl}$. The contribution of spin-orbit coupling has been included. All quantities are with respect to the reactants. (b) Generalized normal-mode vibrational frequencies as a function of the reaction coordinate, s , for the reaction $\text{CH}_3\text{F} + \text{Cl} \rightarrow \text{CH}_2\text{F} + \text{HCl}$.

coefficients, whereas a barrier height of 11.4 kJ mol^{-1} gives rate constants in agreement with experimental values. Both barriers are lower than the one obtained in the present study (24.5 kJ mol^{-1} including SO coupling).

The V_{MEP} and ΔV_a^G potential energy curves of the OH reaction with CH_3F at the MP2/aug-cc-pVTZ PES and the corresponding curves corrected by the ISPE method are given in Figure 8a; the generalized normal-mode frequencies are given in Figure 8b. The Arrhenius plot of the calculated rate coefficients in comparison to the experimental values for the OH reaction with CH_3F is shown in Figure 9. Like for the reaction with Cl, the effect of spin-orbit coupling of the OH radical was taken into account for the calculation of the rate coefficients. The electronic barrier height was increased by 0.8 kJ mol^{-1} according to the calculated spin-orbit coupling at the stationary points. In contrast to the calculations of the Cl reaction with CH_3F , where the harmonic oscillator approximation was applied for all frequencies in the calculation of the rate coefficients for the OH reaction, the internal $\text{C}\cdots\text{H}\cdots\text{OH}$ torsional mode was treated as a hindered rotor. As can be seen from Figure 9, our TST and CVT/SCT calculations within the ISPE model give rate coefficients in reasonable agreement with experimental data. However, the temperature dependence of the calculated rate coefficients is more pronounced compared to the experimental values. There can be observed experimental

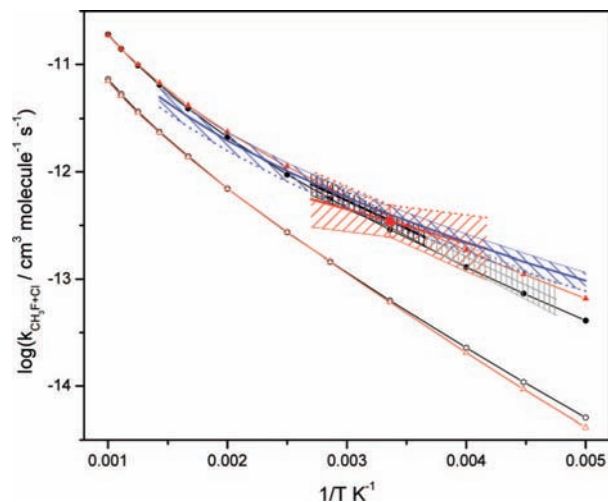


Figure 7. Arrhenius plot of calculated and experimental rate coefficients for the reaction $\text{CH}_3\text{F} + \text{Cl} \rightarrow \text{CH}_2\text{F} + \text{HCl}$. (Δ) This work, ICVT/SCT with ISPE including SO coupling. (\circ) This work, ICVT/SCT with IOE (scaled vibrational frequencies, scaling factor $c = 0.9552$) including SO coupling. (\blacktriangle) This work, TST with ISPE including SO coupling. (\bullet) This work, TST with IOE (scaled vibrational frequencies, scaling factor $c = 0.9552$) including SO coupling. (Blue line) This work, LFP-RF experimental measurements with uncertainty limits. (Black line) Sander et al.,²⁵ evaluation of reference data with uncertainty limits (based on the data of Tschukow-Roux et al.²²). (Red line) Atkinson et al.,²⁶ evaluation of reference data with expanded uncertainty limits corresponding approximately to a 95% confidence level (based on the data of Manning and Kurylo²⁰) and including the value at 298 K with its uncertainty.

disagreement concerning the curvature of the Arrhenius plot. Schmoltnner et al.¹³ and DeMore¹⁵ suggest in their evaluations Arrhenius plots without curvature, whereas Atkinson²⁶ recommends an Arrhenius plot with a small curvature. However, these studies include only a temperature range of 240–480 K. A view of previous theoretical studies shows a diverse picture. Most of the studies fit the barrier to reaction to achieve agreement between calculated and experimental rate constants. Electronic barrier heights of 11.7 ,³² 12.8 ,³² 15.1 ,³⁵ 19.2 ,³² 21.8 ,³¹ and 21.5 kJ mol^{-1} ³⁰ can be found. There is no agreement about the treatment of the $\text{C}\cdots\text{H}\cdots\text{OH}$ torsional mode as a hindered rotor as well as about the contribution of tunneling. Albu et al.³⁵ and Lien et al.³² found in their studies small curvature tunneling dominating the reaction, whereas in the study of Espinosa-García et al.,³¹ large curvature tunnelling is dominating. Schwartz and co-workers³⁰ did not only fit the barrier height but also the imaginary frequency of the saddle point to get results calculated in agreement with experiments. The imaginary frequency influences the barrier width and thus tunnelling. By adjustment of the imaginary frequency, they fit the calculated curvature of the Arrhenius plot to experimental rate constants.

3.2.3. Kinetic Isotope Effects. The calculated ¹³C and ²H kinetic isotope effects in the Cl reaction with CH_3F are given in comparison to experimental data in Table 5. The corresponding calculated KIEs in the temperature range of 200–1000 K are available in Table S7 (Supporting Information). Our ICVT/SCT calculations of the KIE(¹²CH₃F/¹³CH₃F) and KIE(CH₃F/CD₃F) are not able to reproduce the experimental values neither with unscaled nor with scaled frequencies. The ICVT/SCT calculations predict for the CH₃F/CD₃F KIE values that are significantly too low, whereas the carbon-13 KIE is calculated to be larger than the experimental value. In the TST calculations, the obtained CH₃F/CD₃F KIE is significantly larger than the

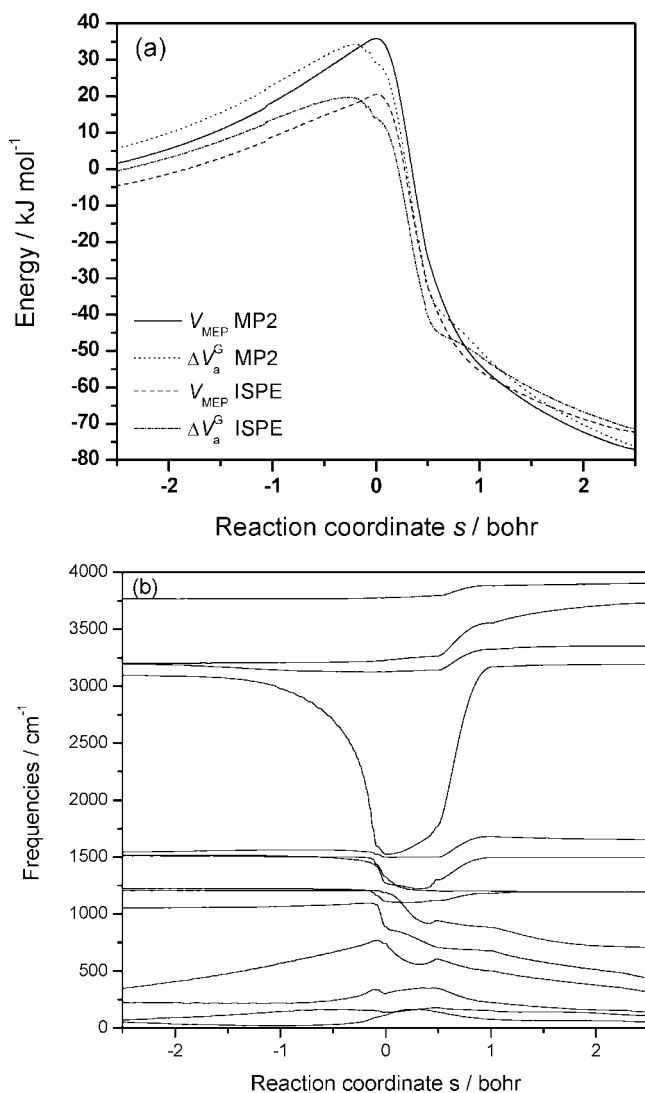


Figure 8. (a) Minimum energy path, V_{MEP} , and vibrationally adiabatic ground-state potential energy curve, ΔV_a^G , as a function of the reaction coordinate, s , for the reaction $\text{CH}_3\text{F} + \text{OH} \rightarrow \text{CH}_2\text{F} + \text{H}_2\text{O}$ calculated at the MP2/aug-cc-pVTZ level of theory without and with dual-level reaction path dynamics by interpolated single-point energies (ISPE), where the contribution of spin-orbit coupling has been included. All quantities are with respect to the reactants. (b) Generalized normal-mode vibrational frequencies as a function of the reaction coordinate, s , for the reaction $\text{CH}_3\text{F} + \text{OH} \rightarrow \text{CH}_2\text{F} + \text{H}_2\text{O}$.

experimental value, whereas the $^{12}\text{CH}_3\text{F}/^{13}\text{CH}_3\text{F}$ KIE is predicted in good agreement with the experimental value.

To analyze the kinetic isotope effects in more detail, a factor analysis as described in refs 91 and 92 was performed but limited to investigations of the variational effect and the tunneling contribution only:

$$\text{KIE} = \frac{k_{\text{light}}}{k_{\text{heavy}}} = \eta_{\text{trans}} \eta_{\text{rot}} \eta_{\text{vib}} \eta_{\text{tun}} \eta_{\text{var}} \propto \eta_{\text{tun}} \eta_{\text{var}} \quad (10)$$

The tunneling contribution is given as $\eta_{\text{tun}} = \kappa^{\text{SCT}}(\text{light}) / \kappa^{\text{SCT}}(\text{heavy})$, i.e., the ratio of the tunneling factors for the light and the heavy isotopologue, and the variational effect is given as $\eta_{\text{var}} = \text{KIE}^{(0)\text{CVT}} / \text{KIE}^{\text{TST}}$, i.e., the ratio of KIEs calculated using variational and conventional transition state theory.

In the case of the $\text{CH}_3\text{F} + \text{Cl}$ reaction, the factor analysis showed that both the variational effect and the tunneling contribution are of similar magnitude for the $^{12}\text{C}/^{13}\text{C}$ KIE for the whole temperature range, as can be seen from Table S9

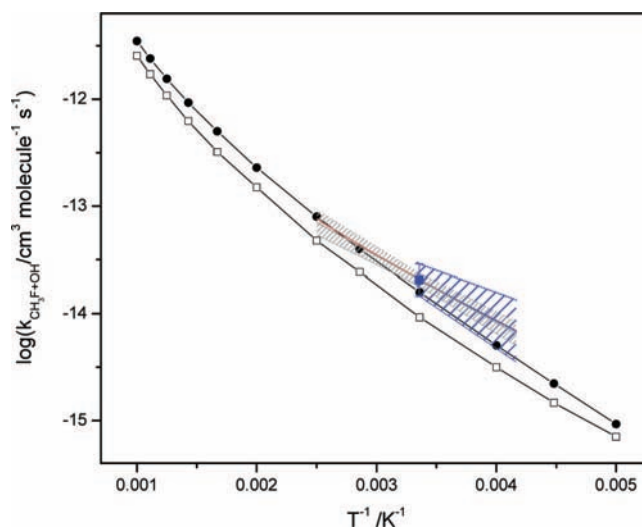


Figure 9. Arrhenius plot of calculated and experimental rate coefficients for the reaction $\text{CH}_3\text{F} + \text{OH} \rightarrow \text{CH}_2\text{F} + \text{H}_2\text{O}$. (□) This work, CVT/SCT with ISPE including SO coupling. (●) This work, TST with ISPE including SO coupling. (Black line) Sander et al.,²⁵ evaluation of reference data with uncertainty limits. (Blue line) Atkinson et al.,²⁶ evaluation of reference data with expanded uncertainty limits corresponding approximately to a 95% confidence level and including the value at 298 K with its uncertainty. (Red line) Atkinson et al.,²⁶ evaluation of reference data using a three-parameter fit.

TABLE 5: Kinetic Isotope Effects, $\alpha = k_{\text{light}}/k_{\text{heavy}}$, in the Reaction of CH_3F with Cl Atoms at 298 K^a

isotopologues	TST	ICVT/SCT		experiment ^b
		unscaled	scaled	
$\text{CH}_3\text{F}/\text{CD}_3\text{F}$	10.7	3.273	3.235	5.11 ± 0.07
$^{12}\text{CH}_3\text{F}/^{13}\text{CH}_3\text{F}$	1.013	1.023	1.033	1.016 ± 0.006
$\text{CH}_3\text{F}/\text{CH}_2\text{DF}$	1.533	1.367	1.360	
$\text{CH}_3\text{F}/\text{CHD}_2\text{F}$	2.850	2.020	2.008	

^a The reaction rates are obtained by direct variational transition state theory with interpolated single-point energies (ISPE) dynamics calculations based on electronic structure information at the MP2/aug-cc-pVTZ level of theory, as explained in the text. In addition, the frequencies are scaled by a factor of 0.9552 within the IOE model to correct the vibrational frequencies within the harmonic approximation. KIEs calculated with conventional transition state theory (TST) and improved canonical variational transition state theory with small-curvature tunneling (ICVT/SCT) are compared with experimental measurements. ^b This work.

(Supporting Information). A large variational effect for all temperatures can be found for the $\text{CH}_3\text{F}/\text{CD}_3\text{F}$ KIE in the present study: $\eta_{\text{var}}(200 \text{ K}) = 0.17$, $\eta_{\text{var}}(298 \text{ K}) = 0.34$, $\eta_{\text{var}}(500 \text{ K}) = 0.53$. The tunneling contribution for the $\text{CH}_3\text{F}/\text{CD}_3\text{F}$ KIE is unexpectedly predicted $\eta_{\text{tun}} < 1$ (Table S10, Supporting Information). The $\text{CH}_3\text{F} + \text{Cl}$ reaction is characterized by a low vibrationally adiabatic barrier height, $\Delta(E^\ddagger + \text{ZPE}) = 7.6 \text{ kJ mol}^{-1}$ at the CCSD(T)/EB43/MP2/aug-cc-pVXZ ($X = \text{T, Q}$) level of theory including the effect of SO coupling. An inspection of the vibrationally adiabatic ground-state PES, ΔV_a^G , of the $\text{CD}_3\text{F} + \text{Cl}$ reaction shows that for the perdeuterated reaction the effective vibrationally adiabatic barrier height is higher compared to the perprotic barrier (see Figure S7, Supporting Information). Additionally, the shape of ΔV_a^G around the saddle point changes considerably. As a consequence, the dynamic bottleneck is also shifted. The increase of ΔV_a^G for the perdeuterated reaction is caused by the difference in ZPEs of the transition state and reactants [$\Delta \text{ZPE} = (\text{ZPE})_{\text{TS}} - (\text{ZPE})_{\text{reactants}}$], which reduces the barrier for the $\text{CH}_3\text{F} + \text{Cl}$

TABLE 6: Kinetic Isotope Effects, $\alpha = k_{\text{light}}/k_{\text{heavy}}$, in the Reaction of CH₃F with OH Radicals at 298 K^a

isotopologues	TST	CVT/SCT	lit. values	experiment ^b
CH ₃ F/CD ₃ F	4.062	1.803	1.45, ^c 1.57, ^d 3.17 ^e	4.067 ± 0.018
¹² CH ₃ F/ ¹³ CH ₃ F	1.019	1.029		1.067 ± 0.006
CH ₃ F/CH ₂ DF	1.355	1.681		
CH ₃ F/CHD ₂ F	1.615	2.172		

^a The reaction rates are obtained by direct variational transition state theory with interpolated single-point energies (ISPE) dynamics calculations based on electronic structure information at the MP2/aug-cc-pVTZ level of theory, as explained in the text. KIEs calculated with conventional transition state theory (TST) and canonical variational transition state theory with small-curvature tunneling (CVT/SCT) are compared with experimental measurements and literature data. ^b This work. ^c Lien et al.,³² CVT/ μ OMT, MP2, barrier height 11.7 kJ mol⁻¹. ^d Lien et al.,³² CVT/ μ OMT, MP2, barrier height 12.8 kJ mol⁻¹. ^e Lien et al.,³² CVT/ μ OMT, PM3, barrier height 19.2 kJ mol⁻¹.

reaction by 5.3 kJ mol⁻¹ more than for the CD₃F + Cl reaction. For comparison, in Figure S7 (Supporting Information) ΔV_a^G of the ¹³CH₃F + Cl reaction is also displayed. As can be seen, there is no change in the barrier height or in the dynamic bottleneck. The changes in the ΔV_a^G and the shifted dynamic bottleneck for the CD₃F reaction result in a different vibrational force field near the dynamic bottleneck and apparently leads to larger tunneling probabilities for the C–D abstraction reaction compared to the C–H abstraction reaction, although normally one expects tunneling to be more important for the lighter hydrogen than for deuterium. Obviously, the small curvature tunneling approximation used in the present study is not able to describe the tunneling properly; the “corner cutting effect” for this reaction takes place over a larger part of the reaction swath than the SCT approximation is able to describe.^{71,93,94} For the KIE(CH₃F/CH₂DF), a weak variational effect can be observed for all temperatures: $\eta_{\text{var}}(298 \text{ K}) = 0.92$ (Table S11, Supporting Information). This effect is slightly increased for the KIE(CH₃F/CHD₂F), where $\eta_{\text{var}}(298 \text{ K}) = 0.74$ can be found (Table S12, Supporting Information). For both KIEs again an unexpected tunneling contribution of $\eta_{\text{tun}} < 1$ is predicted for two of the three possible abstraction reactions.

Table 6 gives the ¹³C and ²H KIEs in the OH reaction of CH₃F in comparison to experimental values. The corresponding calculated KIEs in the temperature range of 200–1000 K are available in Table S8 (Supporting Information). The experimental value of the KIE(CH₃F/CD₃F) is significantly underestimated by our CVT/SCT calculation, whereas the TST calculation reproduces the experimental value excellently. For the KIE(¹²CH₃F/¹³CH₃F), both the CVT/SCT and TST models predict too low calculated values compared to the experimental value. In our calculations, the internal C···H···OH torsional mode was treated as a hindered rotor. Lien et al.,³² who in their study also applied a hindered rotor treatment of the torsional C···H···OH mode, calculated the CH₃F/CD₃F KIEs by applying dual-level variational transition state theory with adopted barrier heights to fit experimental rate constants. In their CVT/ μ OMT calculations based on the MP2/6-31+G* PES applying a barrier of 11.7 and 12.8 kJ mol⁻¹ they calculated KIEs of 1.45 and 1.57, respectively, at 300 K. Their calculations based on a PM3 PES gave a KIE of 3.17 at 300 K. Further, the KIEs obtained at the PM3 PES show a considerable temperature dependence in the range of 200–1000 K, whereas for the calculations based on the MP2 PES only a weak temperature dependence is observed. Our calculations show a moderate temperature dependence between 200 and 1000 K, as can be seen from Table S8 (Supporting Information).

Comparable to the Cl reaction for the ¹²C/¹³C KIE in the OH reaction, only a small variational effect can be observed. The tunneling contribution shows unexpected values of $\eta_{\text{tun}} < 1$ up to 400 K (Table S13, Supporting Information). The variational effect is large ($\eta_{\text{var}}(298 \text{ K}) = 0.41$) for the CH₃F/CD₃F KIE, which was also found by Lien et al.³² In contrast to the Cl reaction, the tunneling contribution for the OH reaction is $\eta_{\text{tun}} > 1$ for temperatures up to 500 K (Table S14, Supporting Information). For the KIE(CH₃F/CH₂DF) and KIE(CH₃F/CHD₂F), weak variational effects are predicted: $\eta_{\text{var}}(298 \text{ K}) = 1.07$ and 1.05, respectively (Tables S15 and S16, Supporting Information). The tunneling contribution is predicted to be $\eta_{\text{tun}} > 1$ for temperatures up to 400 K, except for one abstraction in the reaction of CH₂DF with OH, where $\eta_{\text{tun}} < 1$ can be found for 200 and 223 K. As discussed above, probably the tunneling contribution is significantly underestimated for the CH₃F reaction.

4. Conclusions

The results of the experimental study applying the laser flash photolysis–resonance fluorescence technique to determine the absolute rate coefficients for the reaction of CH₃F with chlorine in the temperature range of 200–700 K can be fitted to a modified Arrhenius expression with significant curvature. Thus, the experimental values are in good agreement with the previous experimental investigations performed by Manning and Kurylo²⁰ between 216 and 296 K and by Tschuikow-Roux et al.^{22,95} between 273 and 368 K, each of which gave an Arrhenius expression with different temperature dependence. Our theoretical calculations of the rate coefficients support the observed curvature of the Arrhenius plot. They show, however, a slightly larger temperature dependence compared to the experimental results.

As seen in Table 1, the ¹²C/¹³C KIE in the OH reaction of CH₃F is like that for the reactions of CH₃Cl and CH₃OH, also an order of magnitude larger than for CH₄. This can be attributed to the difference in the barrier height of the C···H···OH torsional mode. In the transition state of the OH reaction with CH₄, the torsional barrier is only 17 cm⁻¹ at the MP2/aug-cc-pVDZ level of theory, whereas the barrier of the corresponding mode in the transition states of the OH reaction with CH₃F and CH₃Cl are 454 and 303 cm⁻¹, respectively. Since in the hindered rotor scheme we have used the internal rotational axis going through the center of mass of the whole system, the internal rotational mode contributes to the ¹²C/¹³C kinetic isotope effect.

On the basis of the results from this work, the deuterium kinetic isotope effects can be explained by variational effects and tunneling. Our calculations are not able to reproduce the observed values for the deuterium KIEs in the OH and Cl reactions of CH₃F. However, as we have pointed out already, the tunneling method used in this work (SCT) is not able to describe the tunneling effect properly. This is clearly seen in the factor analysis for the perdeuterated species. We expect that the use of a more sophisticated tunneling method will result in better agreement with the experimental observations of the KIEs.

Acknowledgment. This work is part of the ACTION project supported by the Norwegian Research Council under contract 160272/V30. The Norwegian High Performance Computing Consortium is acknowledged for grants of computing time. Research carried out at Georgia Tech was supported by the National Aeronautics and Space Administration through grants NAGW-1001 and NNG06GD90G.

Supporting Information Available: Experimental FTIR spectrum of a $\text{CH}_3\text{F}/^{13}\text{CH}_3\text{F}/\text{Cl}_2$ reaction mixture (Figure S1). Experimental FTIR spectrum of a $\text{CH}_3\text{F}/^{13}\text{CH}_3\text{F}/\text{H}_2/\text{O}_3$ reaction mixture (Figure S2). Experimental FTIR spectrum of a $\text{CH}_3\text{F}/\text{CD}_3\text{F}/\text{Cl}_2$ reaction mixture (Figure S3). The “natural” removal of CH_3F in the reactor (Figure S4). Structures of the stationary points of the $\text{CH}_3\text{F} + \text{Cl} \rightarrow \text{CH}_2\text{F} + \text{HCl}$ reaction (Figure S5) and the $\text{CH}_3\text{F} + \text{OH} \rightarrow \text{CH}_2\text{F} + \text{H}_2\text{O}$ reaction (Figure S6). Vibrationally adiabatic ground-state potential energy curves for the reactions of CH_3F , CD_3F and, $^{13}\text{CH}_3\text{F}$ with Cl with the position of the bottlenecks of the reactions at 298 K indicated (Figure S7). Wavenumber regions and chemical components included in spectral analyses of the different reaction mixtures (Table S1). Structural parameters of the stationary points of the $\text{CH}_3\text{F} + \text{Cl} \rightarrow \text{CH}_2\text{F} + \text{HCl}$ reaction (Table S2) and the $\text{CH}_3\text{F} + \text{OH} \rightarrow \text{CH}_2\text{F} + \text{H}_2\text{O}$ reaction (Table S3). Energetics of the stationary points in the $\text{CH}_3\text{F} + \text{Cl} \rightarrow \text{CH}_2\text{F} + \text{HCl}$ reaction (Table S4) and the $\text{CH}_3\text{F} + \text{OH} \rightarrow \text{CH}_2\text{F} + \text{H}_2\text{O}$ reaction (Table S5) in comparison to literature data. Enthalpies for the Cl and OH reactions of CH_3F in comparison to experimental values (Table S6). Kinetic isotope effects in the temperature range of 200–1000 K in the reaction of CH_3F with Cl atoms (Table S7) and OH radicals (Table S8). Factor analysis of the KIEs in the reaction of CH_3F with Cl atoms: $\text{KIE}(^{12}\text{CH}_3\text{F}/^{13}\text{CH}_3\text{F})$ (Table S9), $\text{KIE}(\text{CH}_3\text{F}/\text{CD}_3\text{F})$ (Table S10), $\text{KIE}(\text{CH}_3\text{F}/\text{CH}_2\text{DF})$ (Table S11), and $\text{KIE}(\text{CH}_3\text{F}/\text{CHD}_2\text{F})$ (Table S12). Factor analysis of the KIEs in the reaction of CH_3F with OH radicals: $\text{KIE}(^{12}\text{CH}_3\text{F}/^{13}\text{CH}_3\text{F})$ (Table S13), $\text{KIE}(\text{CH}_3\text{F}/\text{CD}_3\text{F})$ (Table S14), $\text{KIE}(\text{CH}_3\text{F}/\text{CH}_2\text{DF})$ (Table S15), and $\text{KIE}(\text{CH}_3\text{F}/\text{CHD}_2\text{F})$ (Table S16). This material is available free of charge via the Internet at <http://pubs.acs.org>.

References and Notes

- Gierczak, T.; Talukdar, R. K.; Herndon, S.; Vaghjiani, G. L.; Ravishankara, A. R. *J. Phys. Chem. A* **1997**, *101*, 3125.
- Saueressig, G.; Crowley, J. N.; Bergamaschi, P.; Bruhl, C.; Brenninkmeijer, C. A. M.; Fischer, H. *J. Geophys. Res., [Atmos.]* **2001**, *106*, 23127.
- Feilberg, K. L.; Griffith, D. W. T.; Johnson, M. S.; Nielsen, C. J. *Int. J. Chem. Kinet.* **2005**, *37*, 110.
- D'Anna, B.; Bakken, V.; Beukes, J. A.; Nielsen, C. J.; Brudnik, K.; Jodkowski, J. T. *Phys. Chem. Chem. Phys.* **2003**, *5*, 1790.
- Feilberg, K. L.; Johnson, M. S.; Nielsen, C. J. *J. Phys. Chem. A* **2004**, *108*, 7393.
- Feilberg, K. L.; Sellevag, S. R.; Nielsen, C. J.; Griffith, D. W. T.; Johnson, M. S. *Phys. Chem. Chem. Phys.* **2002**, *4*, 4687.
- Feilberg, K. L.; Johnson, M. S.; Nielsen, C. J. *Phys. Chem. Chem. Phys.* **2005**, *7*, 2318.
- Gola, A. A.; D'Anna, B.; Feilberg, K. L.; Sellevag, S. R.; Bache-Andreassen, L.; Nielsen, C. J. *Atmos. Chem. Phys.* **2005**, *5*, 2395.
- Sellevag, S. R.; Nyman, G.; Nielsen, C. J. *J. Phys. Chem. A* **2006**, *110*, 141.
- Nilsson, E.; Nielsen, C. J.; Johnson, M. S. *J. Phys. Chem. A*, in press.
- Bilde, M.; Wallington, T. J. *J. Phys. Chem. A* **1998**, *102*, 1550.
- Feilberg, L. K.; Gruber-Stadler, M.; Johnson, M. S.; Mühlhäuser, M.; Nielsen, C. J. *J. Phys. Chem. A*. [Online early access]. DOI: 10.1021/jp805643x. Published Online: Oct 9, 2008.
- Schmoltnner, A. M.; Talukdar, R. K.; Warren, R. F.; Mellouki, A.; Goldfarb, L.; Gierczak, T.; McKeen, S. A.; Ravishankara, A. R. *J. Phys. Chem.* **1993**, *97*, 8976.
- Nip, W. S.; Singleton, D. L.; Overend, R.; Paraskevopoulos, G. J. *Phys. Chem.* **1979**, *83*, 2440.
- DeMore, W. B. *J. Phys. Chem.* **1996**, *100*, 5813.
- Hsu, K. J.; DeMore, W. B. *J. Phys. Chem.* **1995**, *99*, 1235.
- Howard, C. J.; Evenson, K. M. *J. Chem. Phys.* **1976**, *64*, 197.
- Jeong, K. M.; Kaufman, F. *J. Phys. Chem.* **1982**, *86*, 1808.
- Wallington, T. J.; Hurley, M. D. *Environ. Sci. Technol.* **1993**, *27*, 1448.
- Manning, R. G.; Kurylo, M. J. *J. Phys. Chem.* **1977**, *81*, 291.
- Hitsuda, K.; Takahashi, K.; Matsumi, Y.; Wallington, T. J. *J. Phys. Chem. A* **2001**, *105*, 5131.
- Tschukow-Roux, E.; Yano, T.; Niedzielski, J. *J. Chem. Phys.* **1985**, *82*, 65.
- Tuazon, E. C.; Atkinson, R.; Corchnoy, S. B. *Int. J. Chem. Kinet.* **1992**, *24*, 639.
- Wallington, T. J.; Ball, J. C.; Nielsen, O. J.; Bartkiewicz, E. J. *Phys. Chem.* **1992**, *96*, 1241.
- Sander, S. P.; Friedl, R. R.; Golden, D. M.; Kurylo, M. J.; Moortgat, G. K.; Wine, P. H.; Ravishankara, A. R.; Kolb, C. E.; Molina, M. J.; Finlayson-Pitts, B. J.; Huie, R. E.; Orkin, V. L. *Chemical Kinetics and Photochemical Data for Use in Atmospheric Studies. Evaluation Number 15; National Aeronautics and Space Administration, Jet Propulsion Laboratory*; California Institute of Technology: Pasadena, CA, 2006.
- Atkinson, R.; Baulch, D. L.; Cox, R. A.; Crowley, J. N.; Hampson, R. F.; Hynes, R. G.; Jenkin, M. E.; Rossi, M. J.; Troe, J.; Wallington, T. J. *Atmos. Chem. Phys.* **2008**, *8*, 4141.
- Xiao, J.-F.; Li, Z.-S.; Liu, J.-Y.; Sheng, L.; Sun, C.-C. *J. Comput. Chem.* **2002**, *23*, 1456.
- Murray, C.; Retail, B.; Orr-Ewing, A. J. *Chem. Phys.* **2004**, *301*, 239.
- Rosenman, E.; McKee, M. L. *J. Am. Chem. Soc.* **1997**, *119*, 9033.
- Schwartz, M.; Marshall, P.; Berry, R. J.; Ehlers, C. J.; Petersson, G. A. *J. Phys. Chem. A* **1998**, *102*, 10074.
- Espinosa-Garcia, J.; Coitino, E. L.; Gonzalez-Lafont, A.; Lluich, J. M. *J. Phys. Chem. A* **1998**, *102*, 10715.
- Lien, P.-Y.; You, R.-M.; Hu, W.-P. *J. Phys. Chem. A* **2001**, *105*, 2391.
- El-Taher, S. *Int. J. Quantum Chem.* **2001**, *84*, 426.
- Korchowiec, J. *J. Phys. Org. Chem.* **2002**, *15*, 524.
- Albu, T. V.; Swaminathan, S. *J. Phys. Chem. A* **2006**, *110*, 7663.
- Aker, P. M.; Sloan, J. J. *J. Chem. Phys.* **1986**, *85*, 1412.
- Huang, Y.; Gu, Y.; Liu, C.; Yang, X.; Tao, Y. *Chem. Phys. Lett.* **1986**, *127*, 432.
- Streit, G. E.; Whitten, G. Z.; Johnston, H. S. *Geophys. Res. Lett.* **1976**, *3*, 521.
- D'Ottone, L.; Bauer, D.; Campuzano-Jost, P.; Fardy, M.; Hynes, A. J. *Phys. Chem. Chem. Phys.* **2004**, *6*, 4276.
- Tyndall, G. S.; Orlando, J. J.; Kegley-Owen, C. S. *J. Chem. Soc., Faraday Trans.* **1995**, *91*, 3055.
- Griffith, D. W. T. *Appl. Spectrosc.* **1996**, *50*, 59.
- Rothman, L. S.; Jacquemart, D.; Barbe, A.; Benner, D. C.; Birk, M.; Brown, L. R.; Carleer, M. R.; Chackerian, C.; Chance, K.; Coudert, L. H.; Dana, V.; Devi, V. M.; Flaud, J. M.; Gamache, R. R.; Goldman, A.; Hartmann, J. M.; Jucks, K. W.; Maki, A. G.; Mandin, J. Y.; Massie, S. T.; Orphal, J.; Perrin, A.; Rinsland, C. P.; Smith, M. A. H.; Tennyson, J.; Tolchenov, R. N.; Toth, R. A.; Vander Auwera, J.; Varanasi, P.; Wagner, G. J. *Quant. Spectrosc. Radiat. Transfer* **2005**, *96*, 139.
- York, D. *Can. J. Phys.* **1966**, *44*, 1079.
- Stickel, R. E.; Nicovich, J. M.; Wang, S.; Zhao, Z.; Wine, P. H. *J. Phys. Chem.* **1992**, *96*, 9875.
- Nicovich, J. M.; Wang, S.; Wine, P. H. *Int. J. Chem. Kinet.* **1995**, *27*, 359.
- Nicovich, J. M.; Wang, S.; McKee, M. L.; Wine, P. H. *J. Phys. Chem.* **1996**, *100*, 680.
- Bilde, M.; Sehested, J.; Nielsen, O. J.; Wallington, T. J.; Meagher, R. J.; McIntosh, M. E.; Pietry, C. A.; Nicovich, J. M.; Wine, P. H. *J. Phys. Chem. A* **1997**, *101*, 8035.
- Ayhens, Y. V.; Nicovich, J. M.; McKee, M. L.; Wine, P. H. *J. Phys. Chem. A* **1997**, *101*, 9382.
- Pietry, C. A.; Soller, R.; Nicovich, J. M.; McKee, M. L.; Wine, P. H. *Chem. Phys.* **1998**, *231*, 155.
- Finlayson-Pitts, B. J.; Pitts, J. N. J. *Chemistry of the Upper and Lower Atmosphere*; Academic Press: San Diego, 2000; p 146.
- Møller, C.; Plesset, M. S. *Phys. Rev.* **1934**, *46*, 618.
- Raghavachari, K.; Trucks, G. W.; Pople, J. A.; Head-Gordon, M. *Chem. Phys. Lett.* **1989**, *157*, 479.
- Montgomery, J. A., Jr.; Frisch, M. J.; Ochterski, J. W.; Petersson, G. A. *J. Chem. Phys.* **1999**, *110*, 2822.
- Montgomery, J. A., Jr.; Frisch, M. J.; Ochterski, J. W.; Petersson, G. A. *J. Chem. Phys.* **2000**, *112*, 6532.
- Frisch, M. J.; Trucks, G. W.; Schlegel, H. B.; Scuseria, G. E.; Robb, M. A.; Cheeseman, J. R.; Montgomery, J. A., Jr.; Vreven, T.; Kudin, K. N.; Burant, J. C.; Millam, J. M.; Iyengar, S. S.; Tomasi, J.; Barone, V.; Mennucci, B.; Cossi, M.; Scalmani, G.; Rega, N.; Petersson, G. A.; Nakatsuji, H.; Hada, M.; Ehara, M.; Toyota, K.; Fukuda, R.; Hasegawa, J.; Ishida, M.; Nakajima, T.; Honda, Y.; Kitao, O.; Nakai, H.; Klene, M.; Li, X.; Knox, J. E.; Hratchian, H. P.; Cross, J. B.; Adamo, C.; Jaramillo, J.; Gomperts, R.; Stratmann, R. E.; Yazyev, O.; Austin, A. J.; Cammi, R.; Pomelli, C.; Ochterski, J. W.; Ayala, P. Y.; Morokuma, K.; Voth, G. A.; Salvador, P.; Dannenberg, J. J.; Zakrzewski, V. G.; Dapprich, S.; Daniels, A. D.; Strain, M. C.; Farkas, O.; Malick, D. K.; Rabuck, A. D.; Raghavachari, K.; Foresman, J. B.; Ortiz, J. V.; Cui, Q.; Baboul, A. G.; Clifford, S.; Cioslowski, J.; Stefanov, B. B.; Liu, G.; Liashenko, A.; Piskorz, P.; Komaromi, I.; Martin, R. L.; Fox, D. J.; Keith, T.; Al-Laham, M. A.; Peng, C. Y.;

Nanayakkara, A.; Challacombe, M.; Gill, P. M. W.; Johnson, B.; Chen, W.; Wong, M. W.; Gonzalez, C.; Pople, J. A. *Gaussian 03*, Revision B.03; Gaussian, Inc.: Pittsburgh, PA, 2003.

(56) Amos, R. D.; Bernhardtsson, A.; Berning, A.; Celani, P.; Cooper, D. L.; Deegan, M. J. O.; Dobbyn, A. J.; Eckert, F.; Hampel, C.; Hetzer, G.; Knowles, P. J.; Korona, T.; Lindh, R.; Lloyd, A. W.; McNicholas, S. J.; Manby, F. R.; Meyer, W.; Mura, M. E.; Nicklass, A.; Palmieri, P.; Pitzer, R.; Rauhut, G.; Schütz, M.; Schumann, U.; Stoll, H.; Stone, A. J.; Tarroni, R.; Thorsteinsson, T.; Werner, H.-J. *MOLPRO, a package of ab initio programs designed by H.-J. Werner and P. J. Knowles*, version 2002.6; 2002.

(57) Knowles, P. J.; Hampel, C.; Werner, H. J. *J. Chem. Phys.* **1993**, *99*, 5219.

(58) Knowles, P. J.; Hampel, C.; Werner, H.-J. *J. Chem. Phys.* **2000**, *112*, 3106.

(59) Watts, J. D.; Gauss, J.; Bartlett, R. J. *J. Chem. Phys.* **1993**, *98*, 8718.

(60) Dunning, T.H., Jr. *J. Chem. Phys.* **1989**, *90*, 1007.

(61) Kendall, R. A.; Dunning, T. H., Jr.; Harrison, R. J. *J. Chem. Phys.* **1992**, *96*, 6796.

(62) Halkier, A.; Helgaker, T.; Jorgensen, P.; Klopper, W.; Koch, H.; Olsen, J.; Wilson, A. K. *Chem. Phys. Lett.* **1998**, *286*, 243.

(63) Gonzalez, C.; Schlegel, H. B. *J. Phys. Chem.* **1990**, *94*, 5523.

(64) Corchado, J. C.; Coitino, E. L.; Chuang, Y.-Y.; Fast, P. L.; Truhlar, D. G. *J. Phys. Chem. A* **1998**, *102*, 2424.

(65) Gonzalez-Lafont, A.; Villa, J.; Lluch, J. M.; Bertran, J.; Steckler, R.; Truhlar, D. G. *J. Phys. Chem. A* **1998**, *102*, 3420.

(66) Chuang, Y.-Y.; Corchado, J. C.; Truhlar, D. G. *J. Phys. Chem. A* **1999**, *103*, 1140.

(67) Chuang, Y.-Y.; Truhlar, D. G. *J. Phys. Chem. A* **1997**, *101*, 3808.

(68) Corchado, J. C.; Chuang, Y.-Y.; Fast, P. L.; Villà, J.; Hu, W.-P.; Liu, Y.-P.; Lynch, G. C.; Nguyen, K. A.; Jackels, C. F.; Melissas, V. S.; Lynch, B. J.; Rossi, I.; Coitino, E. L.; Fernandez-Ramos, A.; Ellingson, B. A.; Pu, J.; Albu, T. V.; Zheng, J.; Steckler, R.; Garrett, B. C.; Isaacson, A. D.; Truhlar, D. G. *POLYRATE-version 9.6*; University of Minnesota: Minneapolis, MN, 2007.

(69) Isaacson, A. D.; Sund, M. T.; Rai, S. N.; Truhlar, D. G. *J. Chem. Phys.* **1985**, *82*, 1338.

(70) Garrett, B. C.; Truhlar, D. G. *J. Phys. Chem.* **1979**, *83*, 1052.

(71) Liu, Y.-P.; Lynch, G. C.; Truong, T. N.; Lu, D.-H.; Truhlar, D. C.; Garrett, B. C. *J. Am. Chem. Soc.* **1993**, *115*, 2408.

(72) Garrett, B. C.; Truhlar, D. G.; Grev, R. S.; Magnuson, A. W. *J. Phys. Chem.* **1980**, *84*, 1730.

(73) Fast, P. L.; Corchado, J. C.; Truhlar, D. G. *J. Chem. Phys.* **1998**, *109*, 6237.

(74) Berning, A.; Schweizer, M.; Werner, H. J.; Knowles, P. J.; Palmieri, P. *Mol. Phys.* **2000**, *98*, 1823.

(75) Chuang, Y.-Y.; Truhlar, D. G. *J. Chem. Phys.* **2006**, *124*, 179903/1.

(76) *Computational Chemistry Comparison and Benchmark DataBase (CCCBDB), NIST Standard Reference Database 101*; National Institute of Standards and Technology, 2005.

(77) Wallington, T. J.; Hurley, M. D.; Schneider, W. F.; Sehested, J.; Nielsen, O. *J. Chem. Phys. Lett.* **1994**, *218*, 34.

(78) MCPA Software Ltd. *FACSIMILE for Windows*, Version 4.0.31; MCPA Software Ltd.

(79) Gola, A. A.; D'Anna, B.; Feilberg, K. L.; Sellevåg, S. R.; Bache-Andreassen, L.; Nielsen, C. *J. Atmos. Chem. Phys. Discuss.* **2005**, *5*, 3873.

(80) Atkinson, R.; Baulch, D. L.; Cox, R. A.; Crowley, J. N.; Hampson, R. F.; Hynes, R. G.; Jenkin, M. E.; Rossi, M. J.; Troe, J. *Atmos. Chem. Phys.* **2006**, *6*, 3625.

(81) Meagher, R. J.; McIntosh, M. E.; Hurley, M. D.; Wallington, T. J. *Int. J. Chem. Kinet.* **1997**, *29*, 619.

(82) Bednarek, G.; Arguello, G. A.; Zellner, R. *Ber. Der Bunsen-Ges.-Phys. Chem. Chem. Phys.* **1996**, *100*, 445.

(83) Bednarek, G.; Breil, M.; Hoffmann, A.; Kohlmann, J. P.; Mors, V.; Zellner, R. *Ber. Der Bunsen-Ges.-Phys. Chem. Chem. Phys.* **1996**, *100*, 528.

(84) Maul, C.; Haas, T.; Gericke, K.-H.; Comes, F. J. *J. Chem. Phys.* **1995**, *102*, 3238.

(85) Chichinin, A. I. *J. Phys. Chem. Ref. Data* **2006**, *35*, 869, and references therein.

(86) Helgaker, T.; Jørgensen, P.; Olsen, J. *Molecular Electronic-Structure Theory*; John Wiley & Sons Ltd: Chichester, 2000.

(87) Helgaker, T.; Gauss, J.; Jørgensen, P.; Olsen, J. *J. Chem. Phys.* **1997**, *106*, 6430.

(88) Simon, S.; Duran, M.; Dannenberg, J. J. *J. Chem. Phys.* **1996**, *105*, 11024.

(89) Capecechi, G.; Werner, H. J. *Phys. Chem. Chem. Phys.* **2004**, *6*, 4975.

(90) Manthe, U.; Capecechi, G.; Werner, H. J. *Phys. Chem. Chem. Phys.* **2004**, *6*, 5026.

(91) Joseph, T.; Steckler, R.; Truhlar, D. G. *J. Chem. Phys.* **1987**, *87*, 7036.

(92) Corchado, J. C.; Truhlar, D. G.; Espinosa-Garcia, J. *J. Chem. Phys.* **2000**, *112*, 9375.

(93) Skodje, R. T.; Truhlar, D. G.; Garrett, B. C. *J. Phys. Chem.* **1981**, *85*, 3019.

(94) Truhlar, D. G.; Isaacson, A. D.; Garrett, B. C. Generalized transition state theory In *The Theory of Chemical Reaction Dynamics*; Baer, M., Ed.; CRC Press: Boca Raton, FL, 1985; Vol 4, pp 65.

(95) Tschuikow-Roux, E.; Faraji, F.; Paddison, S.; Niedzielski, J.; Miyokawa, K. *J. Phys. Chem.* **1988**, *92*, 1488.

JP807609D